OXFORD

Journal of Petrology, 2025, **66**, egaf002
https://doi.org/10.1093/petrology/egaf002
ADVANCE ACCESS PUBLICATION DATE 9 JANUARY 2025
Original Manuscript

Widespread Occurrence of Former Anhydrite Phenocrysts in Laramide-Age Magmas Related to Porphyry–Skarn Cu Mineralization at Santa Rita and Hanover-Fierro, New Mexico, USA

ANDREAS AUDÉTAT[1,*], JIA CHANG[1,2] and SEAN P. GAYNOR[3,4]

[1]Bavarian Geoinstitute, University of Bayreuth, Universitätsstrasse 30, Bayreuth 95447, Germany
[2]State Key Laboratory of Geological Processes and Mineral Resources, China University of Geosciences, Jincheng Street 68, East Late High-Tech Development Zone, Wuhan 430078, Hubei Province, China
[3]Department of Geosciences, Princeton University, Guyot Hall, Princeton 08544, NJ, USA
[4]United States Geological Survey, Geology, Geophysics & Geochemistry Science Center, MS 973 Denver Federal Center, Denver, CO, USA

*Corresponding author. Tel: +49 (0) 921 55-3713; Fax: +49 (0) 921 55-3769; E-mail: andreas.audetat@uni-bayreuth.de
†Handling Editor: Prof. Christina Wang

Reports of magmatic anhydrite are relatively rare, with only ~30 occurrences documented worldwide so far. However, magmatic anhydrite saturation is difficult to recognize because anhydrite decomposes rapidly in near-surface environments. In most cases, only anhydrite inclusions shielded within other phenocryst phases were able to survive. Alternatively, since anhydrite phenocrysts preserved in fresh volcanic rocks are characteristically intergrown with apatite phenocrysts, the former presence of anhydrite phenocrysts can be recognized based on the occurrence of lath-shaped cavities that show a strong spatial association with apatite phenocrysts. These cavities can be either empty or filled with low-temperature, secondary minerals such as zeolites, carbonates, or microcrystalline silica. A systematic search for the occurrence of such cavities, combined with optical and Raman-spectroscopic identification of anhydrite inclusions preserved within apatite, hornblende and quartz phenocrysts, demonstrates that most of the Laramide-age magmas associated with the Santa Rita and Hanover-Fierro porphyry–skarn Cu (Zn, Mo, Au, Pb) deposits were saturated in magmatic anhydrite. The anhydrite typically coexisted with monosulfide solid solution (MSS), suggesting oxygen fugacities of ~2.0 ± 0.5 log units above the fayalite–magnetite–quartz buffer. The magmas range from andesitic to rhyodacitic in composition, and from shortly pre-mineralization (~61 Ma) to shortly post-mineralization (~57 Ma) in age. In three samples with particularly well-recognizable former anhydrite phenocrysts, their modal abundance could be quantified based on high-resolution scans of polished hand specimens. The observed modal anhydrite abundances of 0.63 to 1.8 vol % translate into minimum magma sulfur contents of 0.20 to 0.56 wt % S. The highest sulfur content of 0.56 wt % S is difficult to reconcile with available anhydrite solubility models, but it could be reproduced in an anhydrite solubility experiment performed at 950°C and 1.15 GPa on a natural latite containing 13.1 wt % dissolved H_2O. The sample with the second-highest sulfur content of 0.26 wt % S requires ~10 wt % H_2O in the silicate melt, and, consequently, a minimum pressure of ~0.5 GPa. Taken together, the results suggest that the magmas of the Central Mining District were extremely hydrous and thus originated from great depth. Indeed, their major element compositions and reconstructed H_2O and S contents agree well with experimentally observed and numerically predicted compositions of residual silicate melts after 50 to 70 wt % crystallization of ordinary arc basalts at high pressure and high oxygen fugacities.

Key words: Magmatic anhydrite; Porphyry copper; Sulfur; Sulphur; Magma

INTRODUCTION

Magmatic anhydrite has been described from ca. 30 magma systems worldwide, all of which occur in arc settings (Table 1). However, its former presence is difficult to demonstrate because anhydrite decomposes rapidly in near-surface environments. Luhr *et al.* (1984) reported that anhydrite phenocrysts present in volcanic ashes sampled two weeks after the 1982 eruption of El Chichón volcano in Mexico, had already vanished after a single rainy season. For this reason, evidence for the former presence of anhydrite in fossil magma systems stems mostly from rare anhydrite inclusions within other phenocrysts, where they were shielded from near-surface waters (Luhr *et al.*, 1984; Luhr, 2008). On the other hand, due to the strong tendency of magmatic anhydrite to be intergrown with apatite microphenocrysts (Fig. 1), any lath-shaped cavities that show a strong spatial association with apatite microphenocrysts and occur in otherwise little-altered rocks may represent former anhydrite phenocrysts. This relation was first recognized by Audétat *et al.* (2004) on a sample from Santa Rita, NM (sample SR08, discussed below) based on the observation that incompletely shielded, lath-shaped inclusions next to completely shielded anhydrite inclusions within apatite were filled with the same orange-colored, microcrystalline SiO_2 powder as those present in larger cavities spatially associated with apatite microphenocrysts. Magmatic anhydrite was later described from four more samples from Santa Rita (Audétat & Pettke, 2006). In the present study, we show that virtually all

RECEIVED JULY 24, 2024; **REVISED** DECEMBER 11, 2024; **ACCEPTED** DECEMBER 14, 2024

Table 1: Previous reports of magmatic anhydrite

Occurrences	Mineralization	References
Volcanic rocks (n = 13)		
Aucanquilcha, Chile	none	Hutchinson & Dilles (2019)
Cerro La Lanza, Mexico	none	Luhr (2008)
El Chichón, Mexico	none	Luhr *et al.* (1984); Rose *et al.* (1984); Luhr (2008)
Julcani, Peru	none	Drexler & Munoz (1985); Luhr (2008)
Volcán Lascar, Chile	none	Matthews *et al.* (1994, 1997); Luhr (2008)
Mount Lamington, Papua New Guinea	none	Arculus *et al.* (1983); Luhr (2008)
Nevado del Ruiz, Colombia	none	Fournelle *et al.* (1996); Melson *et al.* (1990); Luhr (2008)
Mount Pinatubo, Philippines	none	Imai *et al.* (1993); Luhr & Melson (1996); Pallister *et al.* (1996)
Redoubt Volcano, USA	none	Swanson & Kearney (2008)
San Juan volcanic field, USA	none	Parat *et al.* (2002, 2005); Luhr (2008)
Sheveluch Volcano, Russia	none	Dirksen *et al.* (2006); Luhr (2008)
Sutter Buttes, USA	none	Luhr (2008)
Yanacocha mining district, Peru	epithermal Au; porphyry Cu–Au	Chambefort *et al.* (2008)
Intrusive rocks (n = 15)		
Bingham Canyon deposit, USA	porphyry Cu–Au–Mo	Zhang & Audétat (2017); Grondahl & Zajacz (2017)
Black Mt deposit, Philippines	porphyry Cu–Au	Cao *et al.* (2018)
Cajon Pass, USA	none	Barth & Dorais (2000); Luhr (2008)
Cerro de Pasco deposit, Peru	epithermal Pb-Zn-Ag	Rottier *et al.* (2020)
Christmas deposit, USA	porphyry Cu	Hutchinson & Dilles (2019)
Duolong deposit, China	porphyry Cu–Au	Li *et al.* (2021)
El Salvador deposit, Chile	porphyry Cu	Hutchinson & Dilles (2019)
El Teniente deposit, Chile	porphyry Cu	Stern *et al.* (2007); Luhr (2008)
Encuentro deposit, Chile	porphyry Cu–Mo–Au	Hutchinson & Dilles (2019)
Grasberg deposit, Indonesia	porphyry Cu–Au	Sulaksono *et al.* (2021)
Middle Urals, Russia	none	Pribavkin *et al.* (2013)
Northparkes deposit, Australia	porphyry Cu–Au	Lickfold *et al.* (2003)
Qulong deposit, China	porphyry Cu–Mo	Xiao *et al.* (2012)
Robinson deposit, USA	porphyry Cu–Au	Hutchinson & Dilles (2019)
Santa Rita deposit, USA	Porphyry Cu–Mo–Au	Core *et al.*, 2001; Audétat *et al.* (2004); Audétat & Pettke (2006)
Yerington mining district, USA	Porphyry Cu	Hutchinson & Dilles (2019)
Yulong deposit, China	Porphyry Cu–Mo	Chang *et al.* (2018)

magmas of ~61–57 Ma age in the Santa Rita – Hanover-Fierro area (i.e. the Central Mining District) were saturated in anhydrite, and some contained up to 0.56 wt % sulfur, which indicates very high water contents and thus magma fractionation at high pressure.

GEOLOGY OF THE CENTRAL MINING DISTRICT

The Central Mining District is composed of (1) the giant Santa Rita porphyry–skarn Cu (Zn-Mo-Au-Pb-Ag) deposit (3.0 Gt ore @ 0.47 wt % Cu, 0.008 wt % Mo, 0.06 g/t Au; 1.4 g/t Ag; Mutschler *et al.*, 1999; Singer *et al.*, 2008), centered on the composite Santa Rita granodiorite porphyry stock, (2) the large Continental Mine skarn-type Cu–Fe (Au, Ag) deposit (also called Hanover Mt. deposit; 1.4 Gt ore @ 0.34 wt % Cu, 0.01 g/t Au, 9.5 g/t Ag; Mutschler *et al.*, 1999; Singer *et al.*, 2008), located at the northwestern margin of the Hanover-Fierro pluton, (3) numerous smaller replacement-style and vein-type Cu–Fe–Zn–Ag–Pb deposits in the sediments around these two intrusions, plus (4) a few Cu–Mo mineralized breccia pipes (Einaudi, 1982; Hernon & Jones, 1986; Hillesland *et al.*, 1995; Thoman *et al.*, 2006; Hannink, 2010). Available zircon U–Pb ages (Mizer *et al.*, 2015; plus own, unpublished data) and molybdenite Re-Os ages (Hannink, 2010) suggest that all these deposits formed between ~61 and ~57 Ma during the Laramide orogeny.

According to the seminal work of Hernon *et al.* (1964) and Jones *et al.* (1967) and recent geochronology data of Mizer *et al.* (2015), Laramide magmatism in the Central Mining District started at 59.5 ± 0.8 Ma with the intrusion of voluminous sills and laccoliths of syenodioritic to quartz dioritic compositions into the Paleozoic and Mesozoic sediments (limestone, sandstone, shale, dolomite) (Fig. 2; Table 2). Subsequently, small andesite and trachyte sills and a few mafic dikes were emplaced. This was followed by the emplacement of multiphase intrusions at Santa Rita (59.8 ± 1.2 Ma) and Hanover-Fierro (58.5 ± 0.9 Ma), which are granodioritic in composition and are genetically associated with the bulk of the mineralization. At approximately the same time, numerous granodiorite porphyry dikes were emplaced at 58.7 ± 0.7 Ma within a 3 km wide corridor that extends from west of the Santa Rita stock to the north of the Hanover-Fierro pluton. Some dikes terminate at the contact to the Hanover-Fierro pluton, other dikes cut it, and two dikes seem to emanate from the northern rim of the Santa Rita stock. After that, late-mineralization to post-mineralization porphyry dikes of quartz monzonitic (58.3 ± 0.8 Ma), quartz latitic, latitic, rhyodacitic (59.0 ± 0.7 Ma; our own data suggest ~57.0 Ma) and rhyolitic composition were emplaced in the same corridor, with the largest number of dikes being present within the Hanover-Fierro pluton and a few kilometers SSW of it (Fig. 2; Table 2). Because we had difficulties with the classification of rhyodacite porphyry dikes and quartz latite porphyry dikes used by Hernon *et al.* (1964) and Jones *et al.* (1967), we used our own criteria to classify this group of rocks: latite porphyry dikes only contain small phenocrysts of mafic minerals and plagioclase; quartz latite porphyry dikes are similar to latite porphyry dikes but contain a few, usually large, quartz phenocrysts; rhyodacite porphyry dikes contain generally larger phenocrysts, including quartz and potassic feldspar; rhyolite porphyry dikes contain very abundant quartz

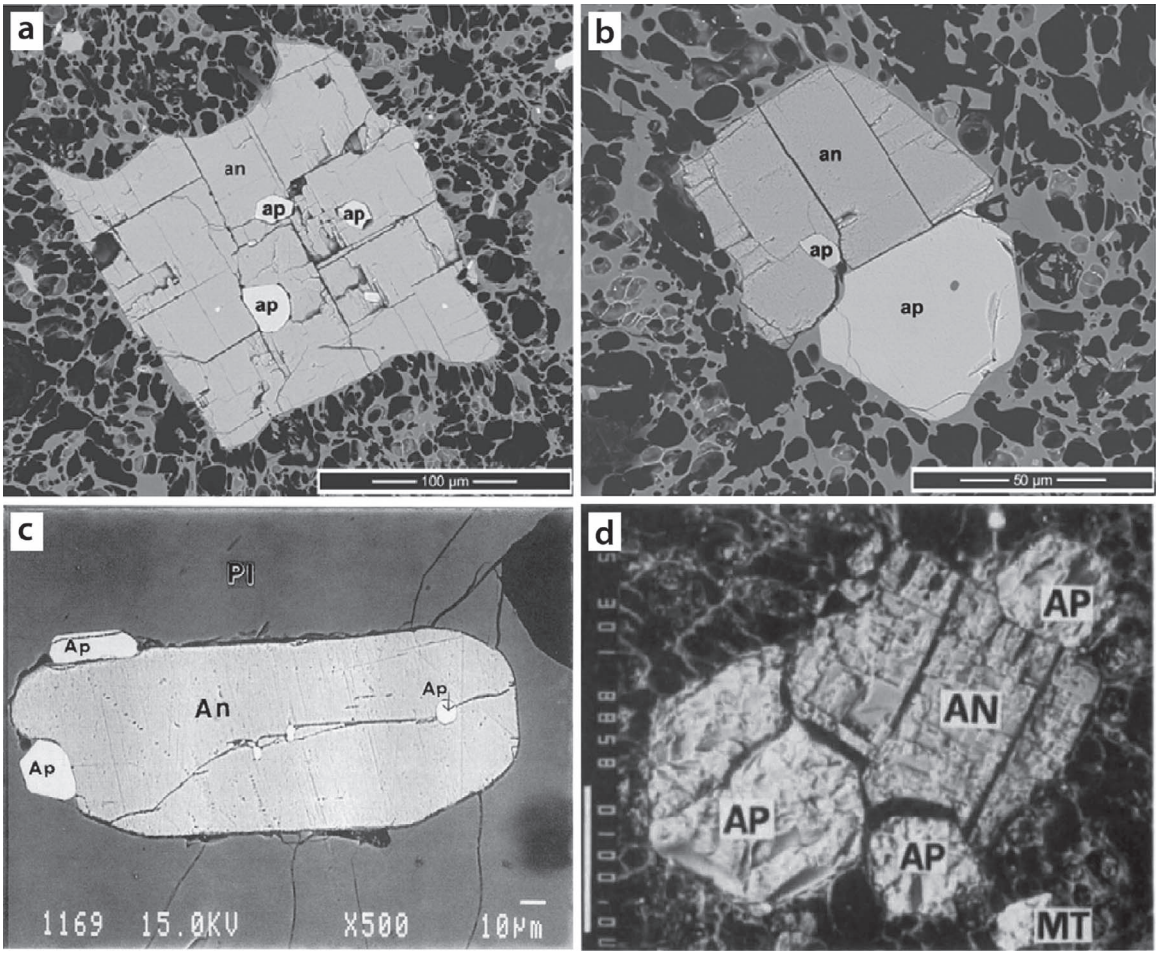

Fig. 1. Characteristics of magmatic anhydrite phenocrysts in fresh volcanic rocks. (a, b) Magmatic anhydrite phenocrysts in pumice of the 1982 El Chichón eruption, Mexico (images reproduced with permission from Luhr, 2008). (c, d) A large, plagioclase-hosted anhydrite inclusion and an anhydrite phenocryst in pumice of the 1991 Mount Pinatubo eruption, Philippines (image c reproduced with permission from Fournelle *et al.*, 1996; image d reproduced with permission from Bernard *et al.*, 1991). Notice the strong spatial association of anhydrite with apatite in all cases. an, anhydrite; ap, apatite; pl, plagioclase. The scale bar on the lower left side of (d) is 100 µm long.

phenocrysts. In the North Star Basin in the northwest corner of Fig. 2, there is a mafic volcanic plug with radiating mafic dikes. The age of these mafic rocks is controversial, but some seem to predate the above magmas by at least 10 m.y., whereas others are ≥10 m.y. younger (see Supplementary Information). For this reason, and because the older mafic magmas are geochemically distinct from all the other magmas (Fig. 3), they are not discussed in the present study except for reporting their petrography and whole-rock composition.

METHODS

A total of 59 samples were investigated, including ones that were previously discussed in Audétat *et al.* (2004) and Audétat & Pettke (2006). During field work 0.5 to 1.0 kg material was collected from each sample. From the freshest 18 samples ca. 0.25 kg material was sent for whole-rock analyses to the ALS company (Brisbane, Australia; www.alsglobal.com). The analytical procedure involved crushing and pulverizing until 85% of the material had a grain size <75 µm, measuring the loss on ignition on one aliquot of this powder, fusing another powder aliquot with added lithium tetraborate to a glass disc, dissolving the glass in an acid solution, and then measuring both major elements (SiO_2, Al_2O_3, $Fe_2O_{3\,tot}$, CaO, MgO, Na_2O, K_2O, TiO_2, MnO, P_2O_5) and trace elements (Ba, Ce, Cr, Cs, Dy, Er, Eu, Ga, Gd, Hf, Ho, La, Lu, Nb, Nd, Pr, Rb, Sc, Sm, Sn, Sr, Ta, Tb, Th, Tm, U, V, W, Y, Yb, Zr) on this dissolved solution using inductively coupled-plasma mass-spectrometry (ICP-MS).

A portion of the remaining sample material was cut with a diamond saw into slabs of ca. 1-cm thickness. One slice of each sample was polished on silicon carbide paper to a grit size of 280, and then covered with glycerol and scanned at a resolution of 2000 ppi on a standard desktop scanner. From each sample, one to five doubly polished sections of 100 to 200 µm thickness were prepared and studied with a standard petrographic microscope. The focus of this analysis was to determine the modal abundances of the various minerals, including former anhydrite phenocrysts, and on preserved anhydrite inclusions. Only inclusions completely enclosed within their host mineral and not intersected by any cracks of fluid inclusion trails were considered. Presumed anhydrite inclusions were subsequently analyzed by Raman spectroscopy. The utilized system is a Horiba Scientific LabRAM HR800 Laser Raman Spectrometer equipped with a HeNe laser source that generates a wavelength of 632.8 nm. The spectra were collected with an exposure time of 20 s and two accumulations. Anhydrite can be unambiguously identified based on prominent Raman bands at ~1017 cm^{-1} and ~1129 cm^{-1}, and smaller ones at ~416, 499, 627, 675, and 1159 cm^{-1}.

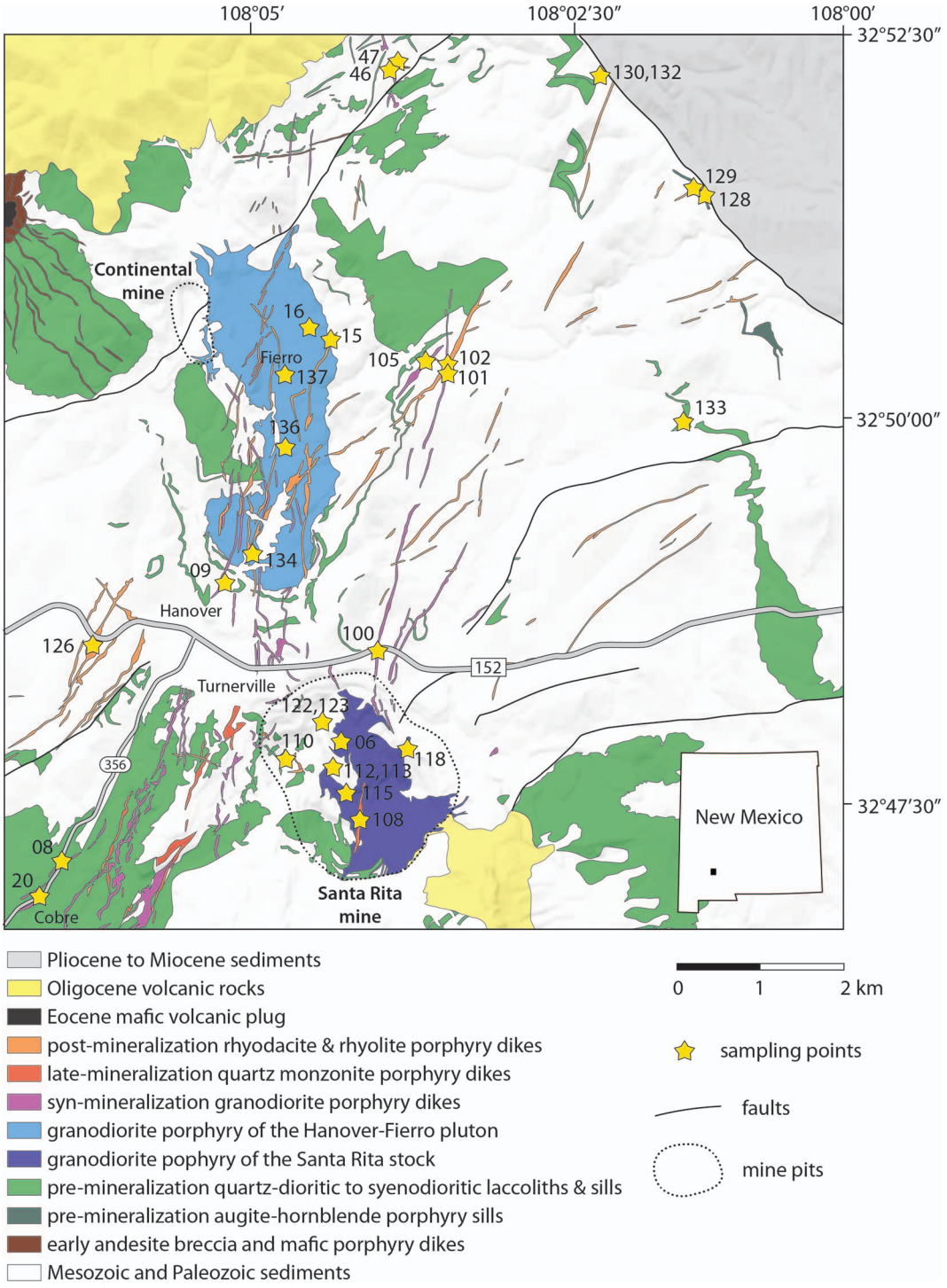

Fig. 2. Simplified geological map of the Central Mining District, modified after Hernon *et al.* (1964), showing the main magmatic units and the sampling points with corresponding sample numbers. Samples 22, 25, 26, 27, 31, and 54, for which only the whole-rock compositions are shown, were sampled outside the displayed area.

Anhydrite solubility experiments were performed on the whole-rock powder of sample SR123a by adding various amounts of distilled H_2O and reagent-grade $CaSO_4{\cdot}2H_2O$. The whole-rock powder was first mixed thoroughly with $CaSO_4{\cdot}2H_2O$ and filled into Au capsules of 5.0 mm outer diameter, 4.6 mm inner diameter, and 7.3 mm length. After adding 6.0 to 10.0 wt % H_2O with a pipette, an Au disc of 4.6 mm diameter and 1.0 mm height was inserted, and then the capsule was compressed in a special vice such that no volatiles could escape during the welding of the top Au lid (Audétat & Bali, 2010). The experiments were performed at 950°C to 1000°C and 0.70 to 1.30 GPa nominal pressure in an end-loaded piston cylinder press, using pure MgO assemblies featuring a graphite heater and a 0.1-mm-thick outermost graphite foil to minimize friction. A friction correction of 0.15 GPa was applied to all experiments, based on calibrations performed with synthetic fluid inclusions in corundum. Temperature

Table 2: Magmatic history of the Central Mining District

Age (Ma)[1]	Unit[2]	Rock type[3]	Age relative to mineralization	Samples
≤46.6 ± 0.9	TKd	Hornblende diorite dikes	>10 m.y. later	25, 27
46.6 ± 0.9	TKg	Orthoclase gabbro plug	>10 m.y. later	not sampled
(59.0 ± 0.7)[4]	Tlq	Rhyolite porphyry dikes	post-min.	126
(59.0 ± 0.7)[4]	Tlq + Tli	Rhyodacite porhpyry dikes	post-min.	09, 15, 122, 129
(59.0 ± 0.7)[4]	Tlq + Tli	Latite porphyry dikes	post-min.	102, 123a
(59.0 ± 0.7)[4]	Tlq + Tli	Quartz latite porphyry dikes	late-min.	110
58.3 ± 0.8	Tqm	Quartz monzonite porphyry dikes	late-min.	108, 112, 113, 118
58.5 ± 0.9	Thg	Hanover-Fierro granodiorite pluton	syn-min.	16, 134, 136, 137
58.7 ± 0.7	Tg	Granodiorite porphyry dikes	syn-min.	08, 20, 46, 100, 101, 105
59.8 ± 1.2	Tsq	Santa Rita granodiorite porphyry stock	syn-min.	06, 115, 123b
n.d.	Kt	Trachyte porphyry sills	pre-min.	not sampled
n.d.	Ksy	Syenodiorite porphyry sills	pre-min.	not sampled
60.5 ± 1.5	Klp (Tlp)	Hornblende-quartz diorite sills	pre-min.	130, 133
59.5 ± 0.8	Kep (Tep)	Quartz diorite porphyry sills	pre-min.	132
n.d.	Ka	Augite-hornblende andesite porphyry sills	pre-min.	128
≥71 ± 2 (?)	TKm	Mafic porphyry dikes	>10 m.y. earlier	22, 26, 31, 47
≥71 ± 2	TKab	Andesite breccia	>10 m.y. earlier	54

[1]Zircon LA-ICP-MS U–Pb ages of Mizer *et al.* (2015), except for the TKab unit, the age of which is constrained by crosscutting relations with the Piños Altos stock (71 ± 2 Ma; K-Ar; McDowell, 1971)
[2]Nomenclature according to Hernon *et al.* (1964); with revised nomenclature according to Mizer *et al.* (2015) shown in parentheses
[3]Nomenclature according to Hernon *et al.* (1964) and Jones *et al.* (1967), except for the three rock types listed under Tlq + Tli, which were defined in the present study
[4]Own, unpublished CA-ID-TIMS zircon U–Pb ages suggest 57.0–57.5 Ma

was measured with a Type S thermocouple. Since the sulfur solubilities were measured at the top of the Au capsule next to the thermocouple, the temperature uncertainty should be <10°C. The runs were terminated after 22 to 47 hours by switching off the power, which resulted in a cooling rate of up to 130°C/second. Longitudinal sections through the capsules were mounted in epoxy, polished to a diamond grain size of 1/4 μm, and then coated with a carbon layer of ~12 nm thickness.

Experimental silicate glasses were analyzed with a JEOL JXA-8200 electron microprobe equipped with two TAP crystals, two PET crystals and one LiFH crystal, using 15 kV acceleration voltage, 10 nA current, and a beam defocused to 10 μm. Silicon, Na, K, S, and Fe were measured first, followed by F, Al, Cl, Ca and Mn, and then Mg, P, and Ti. Counting times were 10 s on peak and 5 s on each background (=10/2x5) for Na and K, 20/2x10 for Si, Al, Ti, Fe, Mn, Mg, Ca, and P, and 60/2x30 for F, Cl, and S. The calibration was made on the following standards: albite (Na), andalusite (Al), apatite (P), diopside (Ca) fluorite (F), forsterite (Mg), hematite (Fe), orthoclase (K), quartz (Si), rhodonite (Mn), rutile (Ti), and sodalite (Cl). Sulfur was calibrated on baryte because the experimental glasses were very oxidized (anhydrite stable and no sulfides present; see below). A sulfur-rich andesite glass (sample SA3 of Botcharnikov *et al.*, 2011, containing 0.32 wt % S normalized dry) was analyzed as an unknown, and the results match the reference value within 7%. The low totals of the electron microprobe analyses were used to obtain rough estimates on the water contents of the silicate glasses for comparison with the FTIR analyses (see below). For that purpose, measurements were also performed on a set of basaltic to rhyolitic glasses with known water contents, and based on the results a correction was applied to the unknowns.

The sulfur content of the experimental glasses was also analyzed with a 193 nm ArF Laser (GeolasPro; Coherent, USA) attached to a quadrupole ICP-MS (Elan DRC-e; Perkin Elmer, Canada). The laser fluence at the sample surface was 10 to 20 J/cm^2, and the laser repetition rate was 5 to 10 Hz. The measurements were performed in a rhombic sample chamber with an internal volume of ~8 cm^3, flushed with He gas at a rate of 0.4 l/min, to which 5 ml/min H_2 was subsequently admixed on the way to the ICP-MS. The ICP-MS system was tuned to a ThO/Th oxide formation rate of 0.05% to 0.10% and a rate of doubly charged Ca ions of 0.15–0.20% using measurements of NIST SRM 610 glass. Analyzed isotopes were ^{23}Na, ^{25}Mg, ^{30}Si, ^{32}S, ^{34}S, ^{39}K, ^{43}Ca, ^{49}Ti, ^{55}Mn, ^{57}Fe, using dwell times of 10 to 50 ms per isotope. External standardization of major and minor element concentrations was based on the andesitic GSE-1G glass (USGS; using the reference values listed on the GeoReM webpage), whereas sulfur was standardized on an in-house andesite glass standard that contains 0.43 wt % S, based on electron microprobe analyses. Internal standardization was done by normalizing the sum of all major and minor element oxides to 100 wt %. Test measurements on the andesitic SA3 glass of Botcharnikov *et al.* (2011) returned sulfur concentrations that matches the reference value within 5%.

The H_2O and CO_2 contents of the quenched silicate melts of three samples (Anhy-1, Anhy-3, and Anhy-5) were quantified via FTIR. The measurements were performed on doubly polished sections of 150 μm thickness using a Bruker IDS Fourier-transform spectrometer attached to a Bruker IR-scope 1 microscope. Near-infrared spectra were obtained using a tungsten light source and a Si-coated CaF_2 beam splitter, whereas mid-infrared spectra were obtained using a Globar light source and a KBr beam splitter. All spectra were collected using a narrow-band MCT detector. Total water contents (dissolved as molecular H_2O and OH^-) were determined from the heights of the absorption bands at 5200 cm^{-1} and 4500 cm^{-1}, using absorption coefficients of 1.14 and 1.12 l mol^{-1}·cm^{-1}, respectively, determined by Ohlhorst *et al.* (2001) for a dacite glass with 62.5 wt % SiO_2. Total carbon contents (dissolved as CO_3^{2-} and minor molecular CO_2) were determined from the heights of the absorption bands at 1515 cm^{-1} and 2345 cm^{-1}, respectively, using absorption coefficients of 170 and 1000 l mol^{-1}·cm^{-1}, respectively, estimated from the work of Nowak *et al.* (2003), Behrens *et al.* (2004) and Morizet *et al.* (2002). The peak height of each band was quantified by subtracting the visually best fitting baseline (the latter linear for H_2O, and curved for CO_2). The glass densities were calculated based on the

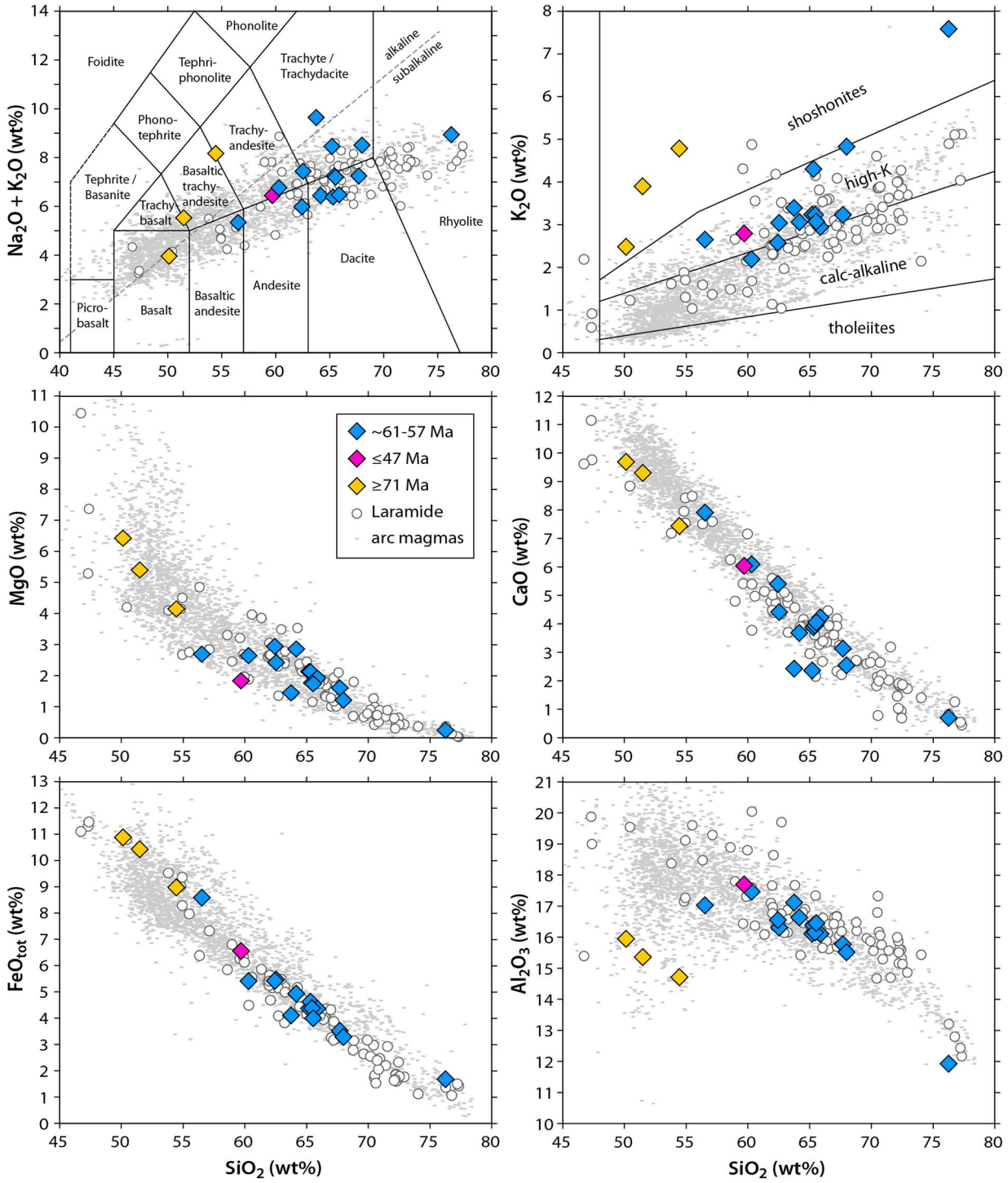

Fig. 3. Whole-rock compositions of samples from the Central Mining District (colored symbols), relative to other Laramide-age intrusives from southwestern USA (open circles; unpublished data) and a global compilation of ordinary arc magmas (gray dots; non-fertile data of Loucks, 2021). The rock nomenclature in the $Na_2O + K_2O$ vs SiO_2 diagram is from Le Bas *et al.* (1986), whereas the alkaline/subalkaline division is from McDonald & Katsura (1964). The samples of the Central Mining District are divided into three age groups: (1) samples that are broadly contemporaneous with the age of mineralization (~61–57 Ma); (2) samples that are at least 10 Ma younger (≤47 Ma), and (3) samples that are at least 10 Ma older (>71 Ma). Notice the shoshonitic nature of the latter samples, which is distinct from the high-K calc-alkaline nature of all other samples.

density model of Ohlhorst *et al.* (2001) for a dacite glass. Uncertainties in the calculated H_2O and CO_2 concentrations are ca. ±0.5 and ± 0.05 wt %, respectively, and include uncertainties associated with the sample thickness (measured with a micrometer), glass density, absorption coefficients, and the reproducibility of the measurements.

RESULTS

Whole-rock chemistry

The major element compositions of 18 whole-rock samples are provided in Table 4. The ~61- to 57-Ma intrusions broadly associated with mineralization contain between 56.5 and 76.3 wt % SiO_2 (normalized dry) and plot in the fields of basaltic andesite,

andesite, trachyandesite (also called latite), dacite, trachydacite, and rhyolite in the total alkalis vs SiO_2 (TAS) diagram (Fig. 3). They are all subalkaline expect for sample SR102, which has an anomalously high Na_2O content, probably due to sodic alteration. In the K_2O vs SiO_2 diagram, they all plot within or very close to the high-K calc-alkaline field, in contrast to the ≥71 Ma magmas, which are clearly shoshonitic. The high K_2O content of aplite sample SR06 likely reflects high-temperature potassic alteration. The ~61- to 57-Ma magmas follow the same major element trends as those of other Laramide-age rocks of southwestern USA (unpublished data from Ajo, Bagdad, Chilito, Christmas, Copper Basin, Crown King, Diamond Joe, Granite Peak, Morenci, Pine Flat, Ray, Safford, San Manuel, Silver King, Tyrone mines) and of global, non-fertile arc magmas (Loucks, 2021) (Fig. 3).

Petrography

An overview of the investigated samples is given in Table 2, and their petrographic characteristics and sample coordinates are provided in Table 3. Scans of selected hand specimens are shown in Fig. 4, whereas the scans of all other samples are provided in Appendix 1. Most samples contain phenocrysts of plagioclase, amphibole, biotite, quartz, magnetite, apatite, and titanite, whereas phenocrystic potassic feldspar, ilmenite, allanite, and/or pyroxene are present only in some samples. In about half of the samples the amphibole, biotite, and plagioclase phenocrysts are altered. Intact amphibole phenocrysts commonly contain sulfide inclusions, whose pyrrhotite-rich composition and commonly platy shape suggest that they were trapped as monosulfide solid solution (MSS). Samples SR15 and SR26 are exceptions to this, containing very small, Cu-rich inclusions that were trapped as sulfide liquid (see also Audétat & Pettke, 2006; Chang & Audétat, 2018). The matrix of all samples is very fine-grained, typically <0.1 mm grain size, and makes up 40 to 90 vol % of the rock (average 60 vol %) (Table 3).

As mentioned in the introduction, the presence of former anhydrite phenocrysts in minimally altered porphyritic rocks can be recognized based on cavities spatially associated with apatite phenocrysts. These cavities can be either empty or they can be filled with low-temperature, secondary minerals, such as zeolites, carbonates, or microcrystalline silica. An exceptionally fresh post-mineralization latite dike sampled within the Santa Rita pit contains anhydrite phenocrysts that are still partly intact and partly replaced by zeolite at their rims (SR123a; Fig. 5a). Sample SR08 (Fig. 5b) is a syn-mineralization granodiorite porphyry that contains particularly well-recognizable former anhydrite phenocrysts. This sample has previously been studied by Audétat *et al.* (2004) and Audétat & Pettke (2006), and the following observations led the authors to conclude that the orange-colored cavities in this sample represent former anhydrite phenocrysts: (i) the strong spatial association of these cavities with apatite phenocrysts; (ii) the occurrence of anhydrite inclusions within apatite-, amphibole- and quartz phenocrysts; and (iii) the fact that lath-shaped, apatite-hosted inclusions that are truncated by cracks are filled with the same orange-colored microcrystalline SiO_2 powder as the one present in the cavities (Figs. 5c, d). The partial replacement of anhydrite phenocrysts by microcrystalline SiO_2 in sample SR123 (Fig. 5a) confirms this conclusion. Examples in which former anhydrite phenocrysts were replaced by zeolite, calcite or siderite are shown in Fig. 5e, 5f and 5g, whereas in the sample shown in Fig. 5h the anhydrite phenocrysts were only dissolved and thus are now represented by empty cavities. Electron microprobe and LA-ICP-MS measurements suggest that the zeolites are variably Sr- and Ba-enriched members of the phillipsite-Ca series.

Anhydrite inclusions are most abundant in apatite phenocrysts, followed by amphibole (in which they are much more difficult to recognize because of the strong coloration of the host, which commonly masks also the characteristically high interference colors of the anhydrite inclusions), plagioclase, and finally quartz. Figure 6 shows five examples of apatite-hosted anhydrite inclusions and one example of amphibole-hosted anhydrite inclusions, together with corresponding Raman spectra to confirm the identity of anhydrite. Additional examples of anhydrite inclusions and corresponding Raman spectra are shown in Appendix 2.

In three samples with particularly well recognizable former anhydrite phenocrysts, their modal abundance was quantified on high-resolution scans (Fig. 7). In the scans of samples SR08 and SR16 the cavities were first outlined by hand, and their total area was then quantified by means of an imaging software (Figs. 7a, b). The empty cavities of sample SR102 (Fig. 5h) were filled with yellow paint prior to the scanning (Fig. 7c), which allowed their abundance to be directly quantified by means of the image processing software without the need to first outline them by hand. The reconstructed abundances of former anhydrite phenocrysts range from 0.63 to 1.75 vol %, which corresponds to sulfur contents of 0.20 to 0.56 wt % S if a magma density of 2.2 g/cm^3 is assumed. The magma density was calculated with the model of Iacovino & Till (2019), using the compositions and reconstructed liquidus temperatures of samples SR137 and SR102 and an average H_2O content of 10 wt % (see below). These sulfur contents are minimum estimates for the bulk magmas because additional sulfur was present in the silicate melt, and because additional sulfur may have been lost an exsolving fluid phase during magma ascent from depth. Sample SR08 represents a physical mixture between a mafic magma and an anhydrite-bearing, dacitic to rhyodacitic magma (Audétat *et al.*, 2004; Audétat & Pettke, 2006), hence the anhydrite content of the felsic endmember must have been substantially higher than the 0.63 vol % of the mixture.

DISCUSSION

Anhydrite phenocrysts in the Hanover-Fierro pluton

Anhydrite was for the first time reported from the Hanover-Fierro pluton by Core *et al.* (2001), where it was described to occur 'in interstices and as inclusions in K-feldspar and quartz' in two samples from a deep drill hole. It is unclear whether the 'interstices' correspond to the former anhydrite phenocrysts identified in the present study, but the preservation of unshielded anhydrite in the deep drill hole confirms the general notion that anhydrite is dissolved by near-surface waters. The former anhydrite crystals identified in samples SR16, SR136, and SR137 clearly represent phenocrysts, as they are much larger than the grains of the matrix (Fig. 7b). The presence of anhydrite phenocrysts in the Hanover-Fierro pluton is significant, as the fluids that produced skarn deposits at its margin appear to have originated from this intrusion. One may thus think that any pre-existing anhydrite phenocrysts should have dissolved during the exsolution of fluids from this magma. However, the following discussion shows that this is not necessarily the case.

The Hanover-Fierro pluton covers an area of ~5 km^2. If all the fluid that produced the Continental skarn deposit at its

Table 3: Sample petrography and sampling coordinates

Sample	Age relative to mineralization	Phenocryst assemblage[1]												Northing[4]	Easting[4]
		total vol%	qtz	plag	Kfsp	bio	amph	cpx	oliv	mgt	ilm	apa	tit	anhy[2]	sulfide incl.[3]		
Hornblende diorite dikes (TKd)																	
SR25	>10 m.y. later	40 ± 5		25			7	7		†		x			**	32.85018	−108.11975
SR27	>10 m.y. later	30 ± 5		20			5	5		†		x			**	32.84828	−108.12150
Rhyolite porphyry dikes (Tlq)																	
SR126	post-min	40 ± 5	10	†	†	2†				?						32.81680	−108.08640
Rhyodacite porphyry dikes (Tli/Tlq)																	
SR09	post-min	20 ± 5	3	†	†	2†	†			†	†	x	†			32.81680	−108.08640
SR15	post-min	40 ± 5	5	20†	5	3†	5			x	x	x	x	m	*	32.84240	−108.07310
SR122	post-min	35 ± 5	5	15	5	†	†			x		x	x	z		32.79939	−108.07734
SR129	post-min	35 ± 5	5	15†	5	†	†			x		x		c		32.85839	−108.02741
Latite porphyry dikes (Tli/Tlq)																	
SR102	post-min	10 ± 5		5†			5			x	x	x		e	**	32.83891	−108.05923
SR123a	post-min	25 ± 5		10			10			3		x	x	x	**	32.79939	−108.07734
Quartz latite porphyry dikes (Tli/Tlq)																	
SR110	late-min	20 ± 5	2	8†	5	3†	3†			x		x	x	c		32.79462	−108.08185
Quartz monzonite porphyry dikes (Tqm)																	
SR108	late-min	35 ± 5	3	17†	7†	5†	3†			x		x	x	m		(32.78603)	(−108.07393)
SR112	late-min	50 ± 5	10	25†	8	5†	3†			†		x	†	s		32.79459	−108.07853
SR113	late-min	30 ± 5	5	15†		5	3†			†		x	x	s		32.79459	−108.07853
SR118	late-min	40 ± 5	7	20†	3	5†	3†			†		x	†	m		32.79566	−108.06849
Hanover-Fierro granodiorite porphyry stock (Thg)																	
SR16	syn-min	50 ± 5	5	30		6	8			x	x	x	x	m		32.84280	−108.07600
SR134	syn-min	80 ± 5	2	60		3	15			x	†					32.81895	−108.08415
SR136	syn-min	40 ± 5	3	27		6	4			x	x	x	x	m		32.83044	−108.07995
SR137	syn-min	50 ± 5	5	30		7	8			x	x	x	x	m		(32.83881)	(−108.08073)
Granodiorite porphyry dikes (Tg)																	
SR08	syn-min	25 ± 5	3	10†	†	5†	5	?†	?†	x	†	x	x	m	*	32.78360	−108.10980
SR20	syn-min	20 ± 5	2	8	†	4†	4	?†	?†	x	†	x	x	c	*	32.78070	−108.11320
SR46	syn-min	40 ± 5	4	18		9†	9†			†		x	x	e		32.87153	−108.06520
SR100	syn-min	45 ± 5	4	20†		10†	10†			†		x	x			32.80886	−108.06549
SR101	syn-min	35 ± 5	1	23†		4†	6†			†		x	†	c		32.83841	−108.05921
SR105	syn-min	45 ± 5	4	20†		10†	10†			x		x	x			32.84061	−108.06032
Santa Rita granodiorite porphyry stock (Tsq)																	
SR06	syn-min	N/A	x	x	x	x				?	x		x			32.79750	−108.07790
SR115	syn-min	50 ± 5	8	25†		5x	12†			?						32.79370	−108.07570
SR123b	syn-min	N/A	x	x	x	x	†					x		z		32.79939	−108.07734
Hornblende-quartz diorite sills (Klp; now Tlp)																	
SR130	pre-min	55 ± 5	2	30			18			5	2	x		z	**	(32.87021)	(−108.03625)
SR133	pre-min	50 ± 5		30†			20†			†				c		32.83315	−108.02785
Quartz diorite porphyry sill (Kep; now Tep)																	
SR132	pre-min	55 ± 5	7	30		5†	10			x	x	x	x	z		(32.87021)	(−108.03625)
Augite-hornblende andesite porphyry sill (Ka)																	
SR128	pre-min	40 ± 5		20			5	10†		5		x			*	32.85831	−108.02690

(Continued)

Table 3: Continued

Sample	Age relative to mineralization	Phenocryst assemblage[1]													Northing[4]	Easting[4]
		total vol%	qtz	plag	Kfsp	bio	amph	cpx	oliv	mgt	ilm	apa	tit	anhy[2]	sulfide incl.[3]	
Mafic porphyry dikes (TKm)																
SR22	>10 m.y. earlier?	30 ± 5		12†				8	4†	5		x			*	32.85293	−108.11900
SR26	>10 m.y. earlier?	35 ± 5		10†				15	5†	5†		x			*	32.84992	−108.12005
SR31	>10 m.y. earlier?	15 ± 5		2†				10	3†	2†		x				32.84819	−108.12172
SR47	>10 m.y. earlier?	15 ± 5		?				10†	?	†						32.87177	−108.06506
Andesite breccia (TKab)																
SR54	>10 m.y. earlier	25 ± 5				4†		18		3		x			*	32.84442	−108.12398

[1]Numbers show the estimated modal abundances of the main phenocryst phases
[2]Anhydrite is replaced by microcrystalline silica (m), zeolite (z), calcite (c), siderite (s), or empty cavities (e)
[3]Abundance of sulfide inclusions: * rare (only a few inclusions per section); ** medium (a few tens of inclusions per section)
[4]WGS84 coordinates; values in parentheses denote grab samples
x, phase is present; ?, presence is uncertain; †, phase is altered; qtz, quartz; plag, plagioclase; Kfsp, potassic feldspar; bio, biotite; amph, amphibole; cpx, clinopyroxene; oliv, olivine; mgt, magnetite; ilm, ilmenite; apa, apatite; tit, titanite; anhy, anhydrite; N/A, not applicable because the rock is either aplitic or equigranular

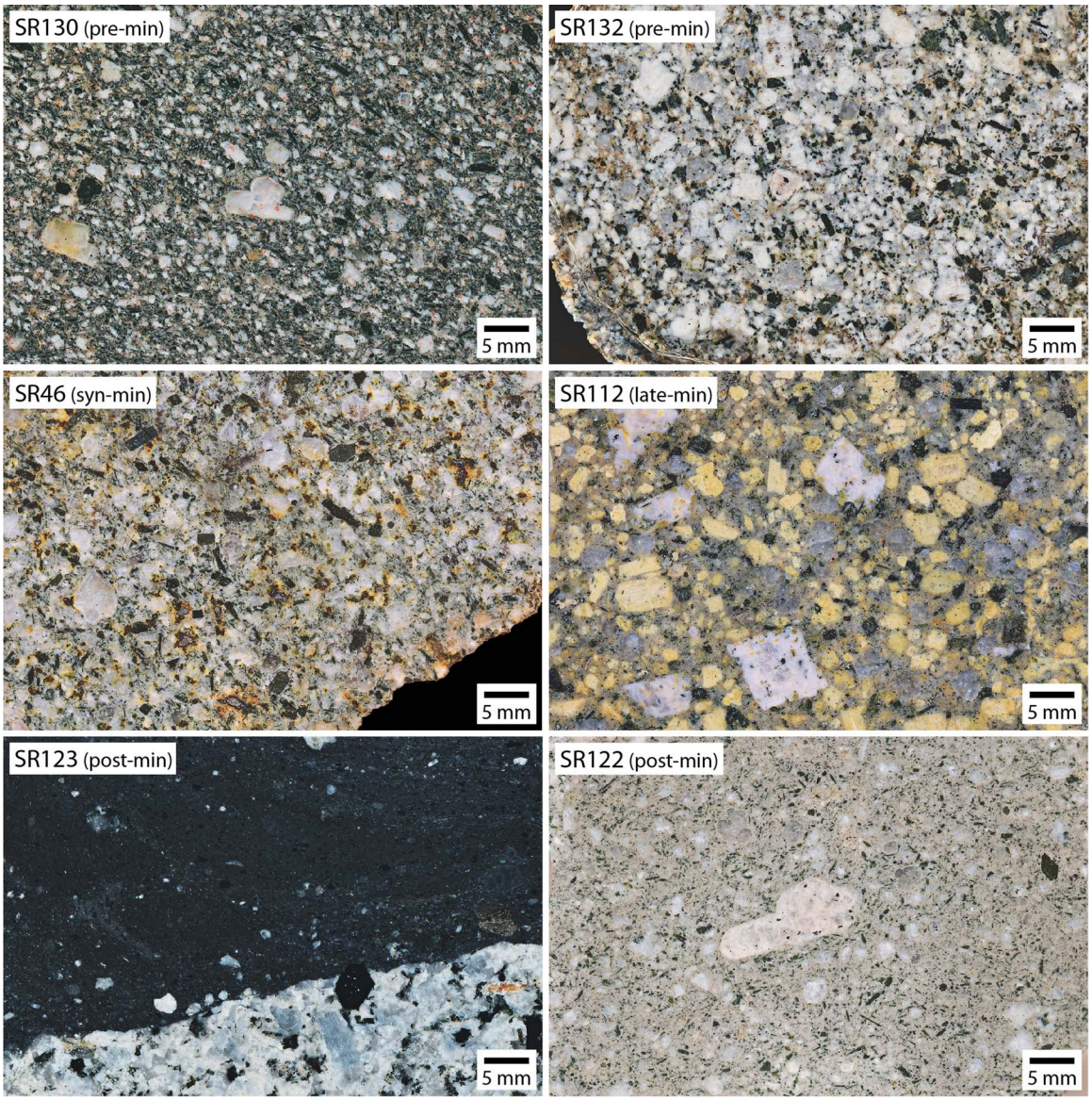

Fig. 4. Scans of selected hand specimens. After cutting with a diamond saw, the samples were polished on 280 grit SiC paper and then covered with glycerol. Sample SR123 shows a dark, fine-grained latite (SR123a) that hosts a coarse-grained granodiorite xenolith (SR123b). Additional scans of all other samples are shown in Appendix 1.

northwestern margin was sourced locally (i.e. from ≤1 km depth below the deposit), it would have been derived from a magmatic volume of max. 5 km^3. This magma volume is far too small to have provided all the fluid and metal that was required to produce the 4.8-Mt Cu contained in the Continental deposit. Assuming a magma density of 2.2 g/cm^3 and a Cu content of ≤100 ppm in the dacitic magma (e.g. Beccaluva *et al.*, 1985; Moss *et al.*, 2001; Jenner *et al.*, 2010, 2015; Park *et al.*, 2015; Keith *et al.*, 2018; Brandl *et al.*, 2023), at least 22 km^3 magma was required to supply all this copper. This is a minimum estimate because (i) most dacitic magmas in the above-cited studies contain less than 50 ppm Cu, (ii) the 4.8 Mt Cu refers only to the *economically mineable* ore, whereas the total Cu mineralization is considerably larger, and (iii) because neither the Cu extraction from the magma nor the Cu precipitation at the site of the ore deposit was likely 100% efficient. A minimum magma volume of 22 km^3 is indicated also by a mass balance for H_2O. For this calculation, it is assumed that the mineralizing bulk fluid contained at most 1000 ppm Cu (Cernuschi *et al.*, 2023) and that the magma contained 10 wt % H_2O (see below). Consequently, most of the ore-forming fluids must have exsolved at greater depth and then have percolated through the currently exposed parts of the Hanover-Fierro pluton. This seems to have happened at (near-) magmatic conditions because the hornblende, biotite, and feldspars in the rocks of the Hanover-Fierro pluton appear fresh (Fig. 7; Appendix 1). The occurrence of anhydrite phenocrysts in rapidly quenched granodiorite dikes of similar age, mineralogy and composition of the Hanover-Fierro pluton implies that the anhydrite phenocrysts were already present at depth. Therefore, any fluids that exsolved from these magmas were already anhydrite-saturated, and during their ascent to the current exposure level of the Hanover-Fierro pluton they likely became anhydrite-oversaturated, due to the decrease of pressure and temperature (Creaser *et al.*, 2022). Hence, there was no reason for these fluids to dissolve existing anhydrite phenocrysts during their percolation through the Hanover-Fierro pluton.

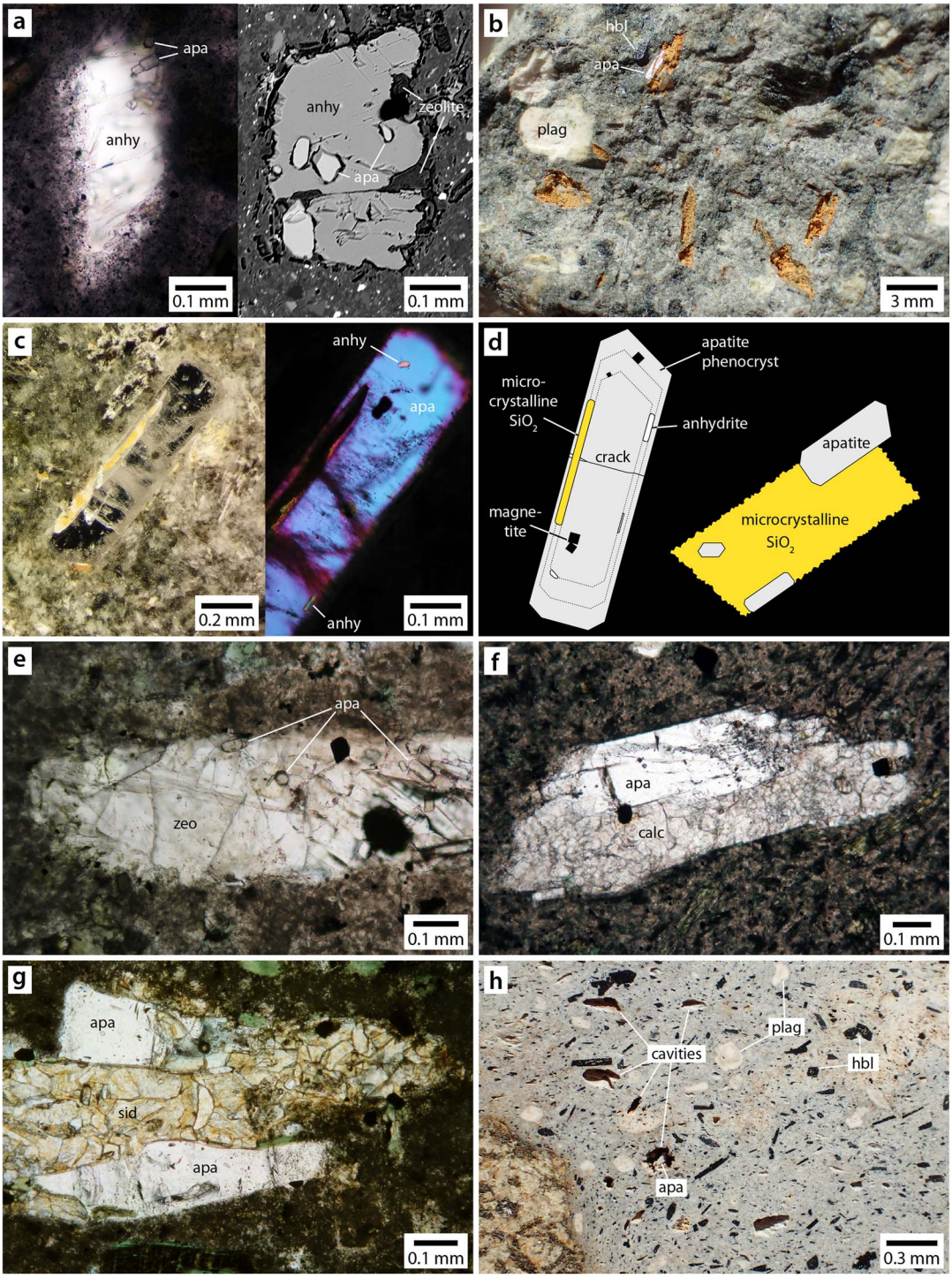

Fig. 5. Petrographic characteristics of preserved and altered anhydrite phenocrysts in rocks of the Central Mining District. (a) Left: transmitted-light photomicrograph of a mostly intact anhydrite phenocryst in a thick section of sample SR123a. Right: reflected-light photomicrograph of another anhydrite phenocryst in the same sample, showing partial replacement of the anhydrite by zeolite. Notice the association of both anhydrite phenocrysts with small apatite microphenocrysts. (b) Photograph of sample SR08, which contains conspicuous, lath-shaped cavities filled with orange-colored, microcrystalline silica. One of them is intergrown with a large apatite phenocryst. Notice the intact nature of plagioclase and hornblende phenocrysts, which prompted the question what former mineral was present in the cavities. (c) Left: binocular view of an apatite phenocryst hosting a large, lath-shaped inclusion that is now replaced by orange-colored, microcrystalline silica. Right: view of the same crystal in cross-polarized transmitted light. A small anhydrite inclusion occurs on the same growth zone as the one along which the large, lath-shaped inclusion filled with microcrystalline silica occurs. (d) Schematic illustration of the relationships shown in panels b and c (modified after Audétat *et al.*, 2004). (e–g) Transmitted-light images of thick-sections in which former anhydrite phenocrysts were replaced by zeolites (e; sample SR122), calcite (f; sample SR20), or siderite (g; sample SR113). (h) Photograph of a cut surface of sample SR102, which contains lath-shaped cavities in otherwise little-altered rock (notice the fresh nature of plagioclase and hornblende crystals). Some of the cavities are associated with apatite phenocrysts. Anhy, anhydrite; apa, apatite; hbl, hornblende; plag, plagioclase; zeo, zeolite; calc, calcite; sid, siderite.

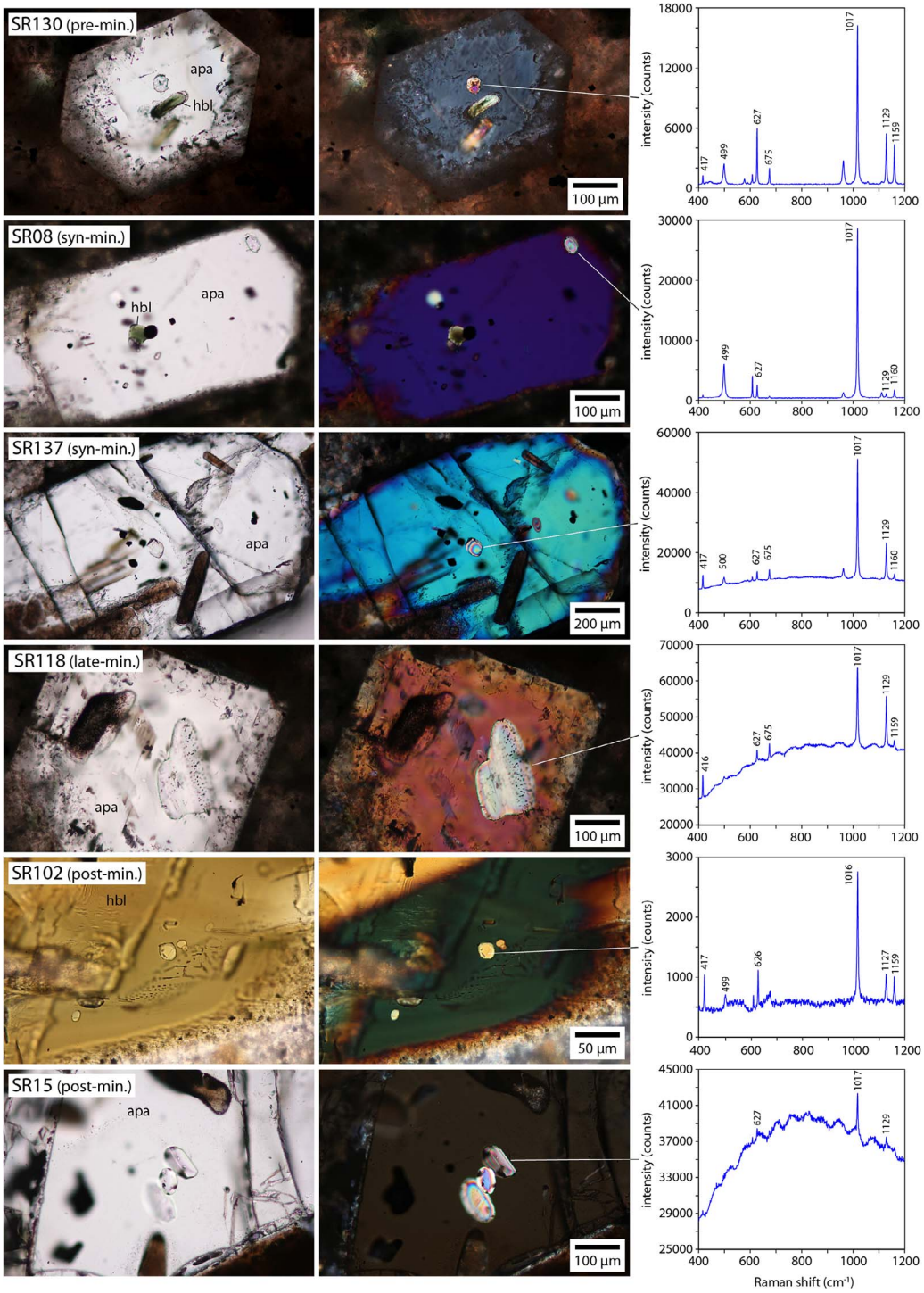

Fig. 6. Transmitted-light and cross-polarized photomicrographs of anhydrite inclusions in apatite and hornblende phenocrysts, plus corresponding Raman spectra. Anhydrite produces prominent Raman bands at ~1017 cm^{-1} and ~ 1129 cm^{-1}, and smaller ones at ~416, 499, 627, 675 and 1159 cm^{-1}. Some apatites are strongly fluorescent, masking less intense bands of anhydrite inclusions. The birefringence of anhydrite ($\Delta = 0.044$) is similar to that of olivine ($\Delta = 0.035$–0.053) or muscovite ($\Delta = 0.036$–0.054). Images and Raman spectra of anhydrite inclusions in other anhydrite-bearing samples are shown in Appendix 2.

Magmatic fO_2, S-, and H_2O content

The presence of anhydrite in arc magmas requires oxygen fugacities of at least 1.5 log units above the fayalite–magnetite–quartz (FMQ) buffer (e.g. Jugo *et al.*, 2010; Botcharnikov *et al.*, 2011; Parat *et al.*, 2011; Matjuschkin *et al.*, 2016; Li *et al.*, 2019). Intact amphibole phenocrysts from the Central Mining District commonly contain also MSS-type sulfide inclusions (Table 3). The fO_2 of these magmas was thus within the anhydrite+MSS stability field, which ranges from ca. 1.5 log units to ca. 2.5 log units above the FMQ buffer (Parat *et al.*, 2011; Li *et al.*, 2019; Kleinsasser *et al.*, 2022). An independent fO_2 estimate was obtained for sample SR102, which contains optically homogeneous magnetite and ilmenite phenocrysts. Electron microprobe analyses of six magnetite phenocrysts and three ilmenite phenocrysts from that sample are

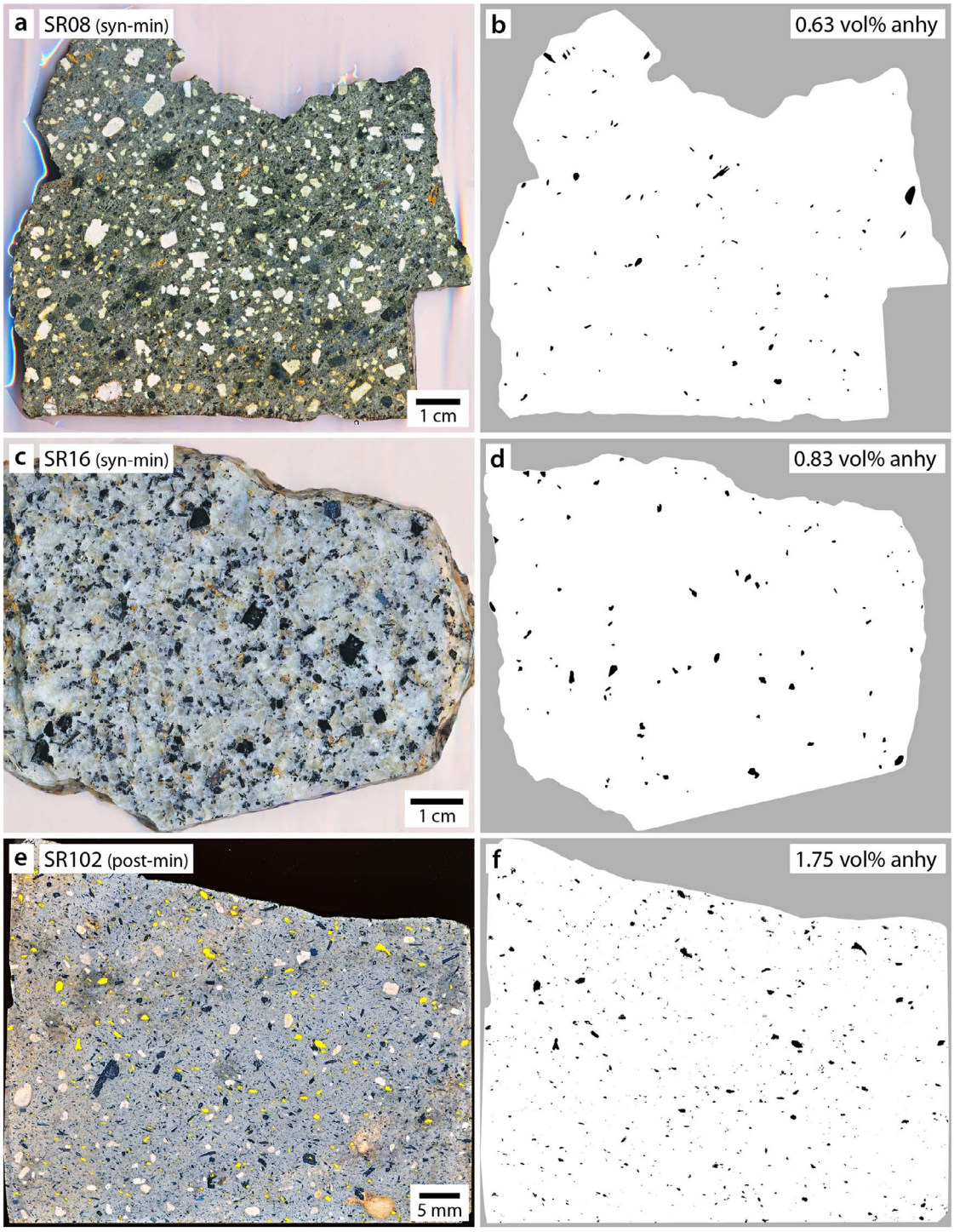

Fig. 7. Scans of polished hand specimens and corresponding illustrations showing the abundance of former anhydrite phenocrysts in black. In sample SR102 the cavities were filled with yellow paint prior to scanning, and the corresponding anhydrite abundance map was produced directly by means of image processing.

presented in the Supplementary Information. The corresponding averages pass the Mg/Mn partitioning test of Bacon & Hirschmann (1988), and return a log fO_2 value of ΔFMQ+2.0 according to the model of Ghiorso & Evans (2008). Temperature cannot be reliably determined from Fe–Ti oxides at these fO_2 conditions because the isotherms are too narrowly spaced (Ghiorso & Evans, 2008).

Magmatic sulfur contents of ≥0.5 wt % S are difficult to reconcile with available anhydrite solubility models. According to the model of Zajacz & Tsay (2019), which currently provides the best fit to published anhydrite solubility data (cf. Xu & Li, 2021; Liu *et al.*, 2023), such high sulfur contents require temperatures of ≥1100°C and water contents of ≥10 wt % H_2O. These temperatures are far too high for the Santa Rita and Hanover-Fierro magmas (see below). On the other hand, the recent studies of Xu & Li (2021) and Xu *et al.* (2022) suggest that the model of Zajacz & Tsay (2019) severely underestimates anhydrite solubilities in melts containing >8 to 9 wt % H_2O (see Supplementary Information for a detailed look at the Xu & Li (2021) data). It should be mentioned that

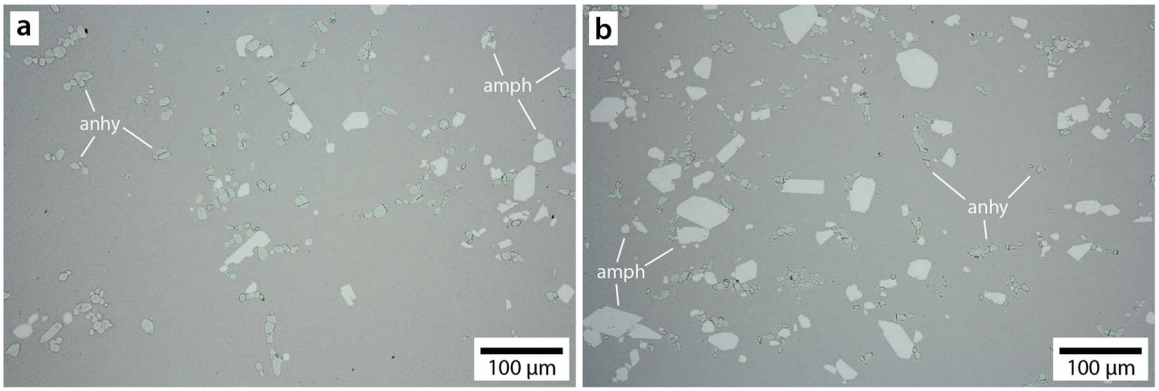

Fig. 8. Reflected-light photomicrographs of samples recovered from two anhydrite solubility experiments performed at 950°C and 1.15 GPa. (a) Anhy-3 with 11.8 wt % H_2O in the silicate melt. (b) Anhy-4 with 10.1 wt % H_2O in the silicate melt.

the Zajacz & Tsay (2019) model was calibrated on melts that contained mostly ≤8.5 wt % H_2O (only 4 out of the 193 data points had higher water contents), hence melts with >8.5 wt % H_2O are out of their calibration range.

For this reason, and because porphyry Cu forming magmas have been proposed to be extremely hydrous (Lu *et al.*, 2015; Loucks, 2021; Loucks & Fiorentini, 2023; Nathwani *et al.*, 2024), we performed six anhydrite solubility experiments on melts of the composition of sample SR123a (i.e. the extraordinarily fresh latite that contains partially preserved anhydrite phenocrysts) with 9.4 to 13.1 wt % dissolved H_2O (Table 5). Sample SR123a is petrographically and compositionally very similar to sample SR102 and was preferred over the latter because it shows no signs of sodic alteration. Both samples contain 63 to 64 wt % SiO_2, 10 to 20 vol % phenocrysts of amphibole, plagioclase, magnetite, apatite and large amounts of (former) anhydrite, although the exact modal abundance of anhydrite phenocrysts in sample SR123a could not be determined because of their partial replacement by zeolite. Due to the relatively low overall phenocryst content of these samples, they should be representative of true silicate liquids, and the abundance and large size of apatite phenocrysts suggests that these liquids were saturated in apatite. Liquidus temperatures were thus estimated with the apatite saturation thermometer of Harrison & Watson (1984), which returned 936°C for SR102 and 956°C for SR123a. Similar apatite saturation temperatures were obtained for samples SR136 (951°C) and SR137 (929°C) from the Hanover-Fierro pluton, which contain 65 to 66 wt % SiO_2. Sample SR137 is petrographically very similar to sample SR16 (Fig. 7b), therefore, the latter melt is assumed to have had a temperature of around 930°C. These temperatures fit well with fractionation experiments on hydrous arc magmas, in which amphibole-saturated melts containing 60 to 65 wt % SiO_2 (normalized dry) are typically obtained in the temperature range of 900°C to 1000°C (e.g. Luhr, 1990; Parat *et al.*, 2008; Freise *et al.*, 2009; Nandedkar *et al.*, 2014; Calvo, 2022). Based on the above information, we performed four of our experiments at 950°C, 1.15 GPa and varied the H_2O content of the melt from 9.4 to 13.1 wt % H_2O. One run was performed at 1000°C to constrain the effect of temperature, and one run was performed at 0.55 GPa to constrain the effect of pressure (Table 5). Images of the quench products of two experiments are shown in Fig. 8, whereas the melt compositions measured by electron probe microanalysis (EPMA), LA-ICP-MS and FTIR are listed in Table 5. Anhydrite was present in all runs except for the first one, where the amount of added $CaSO_4$ was too low to reach anhydrite saturation. Small amounts of amphibole (2–10 vol %) were present in all runs except for the one performed at 1000°C.

The measured sulfur solubilities are summarized in Fig. 9a, where they are compared with anhydrite solubilities predicted for the same melt compositions, H_2O contents and temperatures by the model of Zajacz & Tsay (2019), and with the reconstructed sulfur contents of samples SR16 and SR102. Sample SR08 cannot be used for this comparison because it represents a mixed magma. For the two experiments with 10.0 wt % H_2O dissolved in the silicate melt, our observed anhydrite solubilities are close to those predicted with the model of Zajacz & Tsay (2019). However, for the experiment conducted at 1000°C with 9.4 wt % dissolved H_2O and the two experiments conducted at 950°C with 11.8 and 13.1 wt % dissolved H_2O, our solubility values are higher by factors of 1.4 to 2.0 (Fig. 9b).

If our experimental anhydrite solubility data are taken as reference, then the magma of sample SR16 needed to have contained at least 10 wt % H_2O to dissolve its ~0.26 wt % S, whereas the magma of samples SR102 needed to have contained at least 13 wt % H_2O to dissolve its 0.56 wt % S (Figs. 9a, b). These are minimum estimates, as these melts may not have been saturated in anhydrite when they left their source region. The extraordinarily high water content required for the latter sample suggests that it was derived from a pressure of at least 0.8 GPa (Fig. 9b), i.e. from a lower crustal level. This conclusion is supported by the high Sr/Y-ratio of this sample (Sr/Y = 106; Table 4), which plots far within the fertile field of Loucks (2014, 2021). The underlying assumption in this discussion is that all the former anhydrite phenocrysts present in the samples were originally dissolved in the silicate melt. One may ask whether this is necessarily true, or whether anhydrite phenocrysts could have been extracted together with residual melt during magma fractionation at depth. In order to do so, and in order to preferentially extract anhydrite relative to other phenocrysts, the anhydrite would need to have a lower density than other phenocrysts, and a similar to lower density than the silicate melt. The density of anhydrite at room temperature is 2.97 g/cm^3. At 950°C (i.e. the temperature estimated for sample SR102), its density is ~2.84 g/cm^3 (Evans, 1979). Using the model of Iacovino & Till (2019), the following densities are calculated for the whole-rock composition of sample SR102 at 950°C and 10 kbar (at 5 kbar they would be ~0.1 g/cm^3 lower): 2.27 g/cm^3 with 10 wt % dissolved H_2O, 2.33 g/cm^3 with 8 wt % dissolved H_2O, 2.40 g/cm^3 with 6 wt % dissolved H_2O, 2.47 g/cm^3 with 4 wt % dissolved H_2O, 2.55 g/cm^3 with 2 wt % dissolved H_2O, and 2.64 g/cm^3 with 0 wt % H_2O. In other words, even in the case of a completely dry melt (which is unrealistic) the density of anhydrite would be still considerably higher than that of the melt. For comparison, these are the

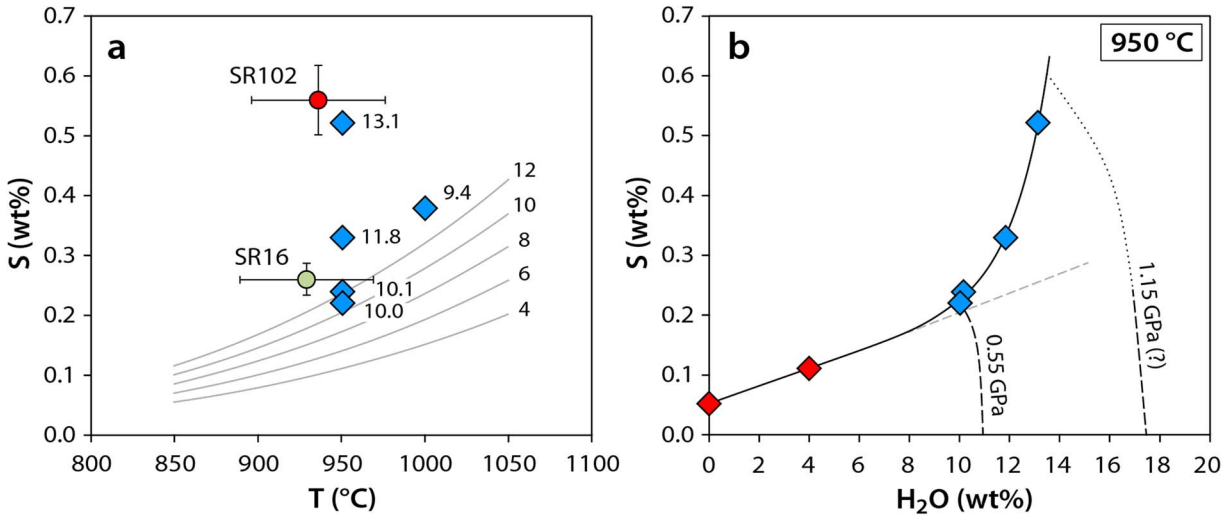

Fig. 9. (a) Diagram showing experimentally determined anhydrite solubilities in the SR123a latite with 9.4 to 13.1 wt % H_2O at 950°C and 0.55–1.15 GPa (blue data points), compared to anhydrite solubilities predicted with the model of Zajacz & Tsay (2019) (gray curves) and reconstructed minimum sulfur contents of samples SR102 and SR16. The numbers next to the blue diamonds and gray curves denote melt H_2O contents in wt %. Whereas the two experiments with 10 wt% H_2O yielded anhydrite solubilities that fit well with those predicted with the model of Zajacz & Tsay (2019), the other three experiments suggest much higher solubilities, particular the one with 13 wt % H_2O. The magma temperature of the two natural samples was constrained via apatite saturation thermometry (Harrison & Watson, 1984) based on whole-rock P_2O_5 and SiO_2 contents. For sample SR16, for which no whole-rock composition is available, the composition of the petrographically very similar sample SR137 was taken instead. The uncertainty associated with the apatite saturation temperatures is about ±40°C (Harrison & Watson, 1984). (b) Schematic diagram showing the dependence of anhydrite solubility in the SR123a latitic melt at 950°C as a function of the melt H_2O content (solid line), plus tentative positions of H_2O-SO_2-CO_2 fluid solubility curves at 0.55 and 1.15 GPa. The blue data points denote anhydrite solubilities determined in the present study, whereas the two red data points and the gray dashed line show anhydrite solubilities predicted for the same melt composition with the model of Zajacz & Tsay (2019). The experiment represented by the lowermost blue data point was performed at 0.55 GPa and was fluid-saturated, whereas the other three experiments shown in blue were performed at 1.15 GPa and were fluid-undersaturated. The melts contained 0.34–0.41 wt % CO_2, and the positions of the pure H_2O-endpoints were calculated with the model of Zhang *et al.* (2007).

densities of common other minerals (Hacker & Abers, 2004; at 950°C; in g/cm^3): beta-quartz = 2.52; albite = 2.56; anorthite = 2.72; orthoclase = 2.51; forsterite = 3.11; enstatite = 3.12; diopside = 3.17; hornblende = 3.15; phlogopite = 2.70. Hence, anhydrite is neither lighter than other phenocrysts, nor similar to lighter than the silicate melt, which renders the scenario of preferential extraction of residual melt together with anhydrite phenocrysts unfeasible.

An obvious question is whether the high sulfur and water contents of the investigated samples are unusual at a global scale, and whether this enrichment could have been the reason for the porphyry–skarn Cu mineralization. Sulfur is needed in magmatic-hydrothermal fluids to eventually precipitate copper-bearing sulfides, but there is generally much more sulfur available than required for that purpose (e.g. Gustafson & Hunt, 1975; Hunt, 1991; Dilles *et al.*, 2015), hence high magmatic sulfur contents do not seem to be helpful regarding metal precipitation efficiency. However, high magmatic sulfur contents require oxidized conditions, and thus are indicative of the suppression of magmatic sulfides that can sequester copper and other chalcophile elements (e.g. Lee *et al.*, 2012; Li & Audétat, 2015; Jenner, 2017), leading to higher metal concentrations in the residual silicate melt. If magma fractionation occurs at high pressure, wherein residual silicate melts can attain very high H_2O contents, the high solubility of both anhydrite and sulfides in such melts may even cause re-dissolution of previously precipitated sulfides, if they are still accessible and not locked away in sulfide-bearing cumulates, further increasing the metal content of the residual silicate melt (Xu *et al.*, 2022). Therefore, high magmatic sulfur contents may indeed be indicative of high metal contents and thus of high mineralization potential, even though studies on natural samples did not find higher copper concentrations in high-Sr/Y magmas compared to low-Sr/Y magmas (e.g. Chiaradia, 2014; Lee & Tang, 2020; Barber *et al.*, 2021).

A high magmatic water content, on the other hand, leads to the exsolution of large amount of fluid from the magma, which may enhance the efficiency of metal extraction from the magma (e.g. Chiaradia & Caricchi, 2017). Furthermore, the magmatic H_2O content controls the depth at which ascending magmas stall and assemble to form upper crustal magma chambers (Huber *et al.*, 2019; Rasmussen *et al.*, 2022), which may be critical for the development of fluid-focusing structures such porphyry fingers and breccia pipes (e.g. Sillitoe, 2010; Audétat & Simon, 2012).

Primitive arc basalts typically contain 3 to 4 wt % H_2O and 0.15–0.2 wt % S (e.g. Wallace, 2005; Métrich & Wallace, 2008; Sadofsky *et al.*, 2008; Wallace & Edmonds, 2011; Plank *et al.*, 2013; Shinohara, 2013; Schmidt & Jagoutz, 2017; Gurenko, 2021). At oxygen fugacities ≥2.0 log units above FMQ buffer, which are commonly reached in arc magmas (e.g. Evans *et al.*, 2012; Bénard *et al.*, 2018), sulfur is dissolved dominantly as sulfate in the silicate melt (Jugo *et al.*, 2010; Botcharnikov *et al.*, 2011; Klimm *et al.*, 2012; Matjuschkin *et al.*, 2016; Kleinsasser *et al.*, 2022) and thus behaves incompatibly during magma fractionation. To produce a residual liquid with 60 wt % SiO_2 through fractionation from a primitive arc basaltic liquid containing 50 wt % SiO_2 and 10 wt % MgO (Schmidt & Jagoutz, 2017), ca. 65 wt % magma crystallization is required (Nandedkar *et al.*, 2014; Ulmer *et al.*, 2018; Calvo, 2022). In the case of 100% incompatible behavior of H_2O and S, this residual liquid with 60 wt % SiO_2 would contain 9 to 12 wt % H_2O and 0.45 to 0.6 wt % S. In reality, concentrations will be lower due to exsolution of CO_2-rich fluids and H_2O incorporation

Table 4: Whole-rock data ($Fe_2O_{3\,tot}$ converted to FeO_{tot}, and then normalized dry)

Sample	SR06	SR15	SR26	SR27	SR31	SR46	SR54	SR102	SR110	SR122	SR123a	SR128	SR129	SR130	SR132	SR134	SR136	SR137
wt %																		
SiO_2	76.26	65.21	51.47	59.69	50.13	64.17	54.44	63.75	65.31	67.70	62.53	56.52	67.98	62.42	65.87	60.30	65.44	65.53
Al_2O_3	11.92	16.12	15.36	17.70	15.95	16.64	14.72	17.12	16.38	15.78	16.32	17.03	15.52	16.56	16.11	17.47	16.16	16.46
FeO_{tot}	1.68	4.38	10.44	6.56	10.88	4.94	8.98	4.10	4.63	3.52	5.47	8.59	3.28	5.42	4.36	5.41	4.39	4.00
CaO	0.70	2.36	9.31	6.04	9.70	3.68	7.44	2.42	3.88	3.14	4.42	7.91	2.54	5.41	4.23	6.09	3.94	4.05
MgO	0.25	2.14	5.41	1.84	6.43	2.86	4.16	1.45	2.13	1.61	2.43	2.70	1.21	2.95	1.93	2.65	1.78	1.74
Na_2O	1.36	5.24	1.64	3.65	1.48	3.39	3.39	6.25	2.09	4.02	4.40	2.70	3.68	3.42	3.54	4.57	4.03	4.13
K_2O	7.59	3.23	3.90	2.80	2.48	3.06	4.79	3.39	4.30	3.23	3.04	2.65	4.83	2.58	2.95	2.19	3.23	3.07
TiO_2	0.11	0.57	1.32	0.89	1.34	0.67	0.97	0.73	0.59	0.46	0.65	0.99	0.43	0.66	0.49	0.64	0.49	0.48
MnO	0.03	0.06	0.18	0.18	0.20	0.11	0.14	0.04	0.12	0.04	0.09	0.18	0.06	0.14	0.11	0.11	0.10	0.10
P_2O_5	0.00	0.43	0.78	0.44	1.01	0.25	0.76	0.35	0.32	0.24	0.36	0.56	0.26	0.24	0.19	0.30	0.22	0.21
SrO	0.01	0.13	0.09	0.11	0.11	0.08	0.08	0.19	0.06	0.11	0.14	0.09	0.05	0.08	0.08	0.12	0.10	0.10
BaO	0.09	0.14	0.10	0.10	0.26	0.15	0.12	0.18	0.18	0.15	0.15	0.08	0.15	0.12	0.14	0.11	0.11	0.12
Total[1]	99.80	94.92	95.39	98.01	94.36	96.15	97.17	98.98	93.71	98.23	98.36	94.83	97.97	96.92	98.08	96.18	99.63	99.95
LOI	1.37	2.72	2.80	1.90	4.37	2.83	2.60	0.95	6.23	3.31	1.94	4.52	3.66	3.51	2.07	0.96	1.18	0.65
μg/g																		
Ba	847	1235	941	898	2270	1355	1130	1495	1490	1270	1270	681	1175	1120	1255	995	922	1020
Ce	30	84	49	58	46	66	72	85	79	68	79	45	64	67	67	79	61	58
Cr	11.0	5.0	53.0	5.0	204.0	51.0	119.0	5.0	<5	<5	<5	5.0	<5	19.0	12.0	18.0	9.0	7.0
Cs	0.7	1.0	0.9	0.7	4.7	0.4	0.6	2.1	1.9	0.4	0.3	1.7	0.9	0.5	0.4	0.3	0.5	0.4
Dy	1.4	3.5	5.8	6.2	5.2	3.9	6.3	2.9	3.2	2.8	3.6	5.3	2.9	4.2	3.9	4.9	3.1	3.3
Er	0.9	1.8	3.3	3.8	2.8	2.4	3.5	1.5	2.0	1.5	2.0	3.2	1.7	2.7	2.4	2.9	2.0	2.0
Eu	0.5	1.7	2.0	2.0	1.9	1.6	2.1	1.6	1.5	1.3	1.6	1.6	1.4	1.5	1.4	1.8	1.2	1.3
Ga	14	24	22	21	19	21	17	20	25	23	24	20	21	21	21	25	22	23
Gd	1.6	4.8	7.2	6.3	6.3	4.7	7.8	4.1	4.4	3.5	4.4	5.6	3.9	4.8	4.3	5.7	3.9	3.9
Hf	1.7	4.5	4.4	5.3	3.4	5.0	5.8	4.3	5.3	4.9	4.8	4.3	3.8	5.3	5.1	6.0	4.8	4.6
Ho	0.3	0.7	1.2	1.2	1.0	0.8	1.2	0.5	0.7	0.5	0.7	1.1	0.6	0.9	0.8	1.0	0.7	0.7
La	18	46	22	27	21	37	34	47	43	38	41	22	39	35	35	37	32	30
Lu	0.2	0.3	0.4	0.6	0.4	0.4	0.5	0.2	0.3	0.2	0.3	0.5	0.3	0.4	0.4	0.4	0.3	0.3
Nb	4.9	9.9	6.4	7.7	5.2	10.0	8.6	7.9	12.8	9.7	13.0	5.9	9.2	8.4	9.6	8.8	8.5	9.1
Nd	12	36	29	32	30	33	43	40	35	29	37	25	32	31	32	42	28	28
Pr	3.5	10.2	6.9	7.9	6.8	8.5	10.2	10.7	9.5	8.1	9.8	6.2	8.7	8.4	8.3	10.7	7.5	7.2
Rb	160	68	111	80	53	75	189	72	111	55	61	68	107	69	83	45	84	85
Sc	2.3	9.5	37.2	13.1	31.3	15.7	29.5	7.2	7.4	5.6	7.7	17.9	5.2	14.6	10.6	13.3	9.7	9.6
Sm	2.1	5.8	7.2	7.1	6.7	6.1	9.2	6.6	5.9	4.7	6.1	5.9	5.3	5.7	5.5	7.9	5.0	5.0
Sn	0.5	1.0	1.4	1.3	1.4	1.1	1.8	0.7	1.4	0.9	1.3	1.1	0.6	1.1	0.8	1.4	0.8	0.7
Sr	172	1010	791	928	939	811	726	1605	500	908	1125	776	429	784	758	1080	814	932
Ta	0.2	0.3	<0.1	0.5	0.2	0.8	0.5	0.3	0.5	0.6	0.4	0.4	0.4	0.4	0.6	0.7	0.3	0.5
Tb	0.3	0.6	1.0	1.0	0.9	0.7	1.1	0.5	0.6	0.5	0.6	0.9	0.5	0.7	0.6	0.8	0.6	0.6
Th	17	7	4	6	4	9	10	7	9	9	9	3	7	7	10	6	9	9
Ti	0.1	0.3	0.8	0.6	0.9	0.4	0.6	0.4	0.4	0.3	0.4	0.6	0.3	0.4	0.3	0.4	0.3	0.3
Tm	0.2	0.3	0.5	0.5	0.4	0.4	0.5	0.2	0.3	0.2	0.3	0.5	0.2	0.4	0.3	0.4	0.3	0.3
U	5.2	2.6	1.9	2.2	1.7	2.3	3.2	1.4	2.2	2.2	2.4	0.8	2.5	1.5	1.6	1.1	2.1	2.4
V	7	84	294	88	333	118	249	75	79	53	89	168	45	121	84	130	87	85
W	1.6	0.9	0.8	1.9	0.6	0.9	0.9	<0.5	3.0	0.5	1.1	<0.5	0.6	<0.5	<0.5	1.3	0.5	<0.5
Y	8	19	31	34	29	24	33	15	18	15	20	30	17	25	23	28	19	20
Yb	0.9	1.6	2.8	3.6	2.5	2.4	3.3	1.5	2.0	1.6	1.9	3.0	1.6	2.6	2.3	2.7	2.1	2.1
Zr	42	162	162	192	116	178	200	157	186	162	171	151	137	189	176	229	167	160
Sr/Y	22	55	25	27	33	34	22	106	28	59	58	26	25	31	34	39	44	47

[1]with Fe as FeO_{tot}; before the normalization to 100 wt %

Table 5: Summary of anhydrite solubility experiments

Experiment	SR123a[1]	Anhy-1		Anhy-2		Anhy-3		Anhy-4		Anhy-5		Anhy-6	
T (°C)		950		950		950		950		1000		950	
P (GPa)		1.15		1.15		1.15		1.15		1.15		0.55	
Duration (hrs)		42		47		41		46		22		39	
Rock powder		SR123a		SR123a		SR123a		SR123a		SR123a		SR123a	
Added gypsum (wt %)		1.2		6.2		6.3		6.4		6.4		6.3	
Added water (wt %)		9.7		9.9		8.0		6.0		6.0		8.1	
Total H_2O (wt %)[2]		11.5		12.7		10.7		8.8		8.9		10.8	
Phases during run		amph		anhy, amph		anhy, amph		anhy, amph		anhy		anhy, amph, mgt, fluid	
vol % crystals		2		3		10		15		5		5	
Melt composition (all values in wt % and normalized dry, except for S, H_2O and CO_2, which are reported wet)													
n[3]		4		4		4		4		4		4	
		Avg	Stdev	Avg	Stdev	Avg	Stdev	avg	Stdev	Avg	Stdev	Avg	Stdev
SiO_2	62.53	62.65	0.32	61.52	0.24	62.97	0.13	64.02	0.29	61.55	0.14	64.15	0.46
TiO_2	0.65	0.66	0.02	0.65	0.02	0.59	0.06	0.54	0.07	0.68	0.02	0.62	0.05
Al_2O_3	16.32	16.25	0.08	16.06	0.12	16.25	0.09	16.53	0.09	16.09	0.09	16.70	0.06
FeO_{tot}	5.47	4.97	0.14	5.12	0.19	4.86	0.10	4.51	0.13	5.20	0.16	3.44	0.18
MnO	0.09	0.10	0.03	0.10	0.03	0.09	0.02	0.08	0.04	0.09	0.02	0.07	0.02
MgO	2.43	1.97	0.05	2.22	0.05	1.85	0.06	1.55	0.09	2.43	0.08	1.93	0.18
CaO	4.42	4.71	0.10	5.29	0.13	4.64	0.04	4.18	0.08	4.97	0.05	4.49	0.17
Na_2O[4]	4.40	4.22	0.73	4.24	0.65	4.29	0.61	4.46	0.67	4.52	0.68	4.61	0.67
K_2O	3.04	3.08	0.08	3.00	0.10	3.15	0.07	3.12	0.12	3.09	0.10	3.17	0.14
P_2O_5	0.36	0.39	0.05	0.32	0.07	0.38	0.03	0.34	0.05	0.42	0.07	0.30	0.07
S by EPMA	n.a.	0.35	0.03	0.53	0.03	0.33	0.02	0.23	0.03	0.35	0.01	0.21	N/A
S by LA-ICP-MS[5]		0.34	0.01	0.51	0.02	0.33	0.03	0.26	0.02	0.42	0.02	0.23	0.02
S predicted[6]		N/A		0.27	0.01	0.23	0.01	0.19	0.01	0.27	0.01	0.18	0.01
H_2O by difference[7]		12.1	0.3	11.4	0.5	11.6	0.2	11.5	0.2	10.3	0.3	10.8	0.20
H_2O by FTIR		11.6	0.1	n.a.		11.8	0.1	n.a.		9.5	0.1	n.a.	
H_2O theoretical[8]		11.7		13.1		11.8		10.1		9.3		N/A	
H_2O preferred		11.6		13.1		11.8		10.1		9.4		10.0 [9]	
CO_2 by FTIR		0.41	0.01			0.34	0.01			0.34	0.02		

[1]Composition of the SR123a starting whole-rock (normalized dry)
[2]Includes the H_2O contained in the rock powder of SR123a (~1.7 wt % H_2O), the added liquid water, and the H_2O in the added gypsum
[3]Number of analyses
[4]Includes a correction for 0.6 wt % Na_2O loss from the very hydrous experimental glasses
[5]The originally normalized dry values were re-calculated wet based on the preferred H_2O values listed below
[6]Sulfur content of the melt at anhydrite saturation predicted by the model of Zajacz & Tsay (2019) (i.e. not normalized dry)
[7]H_2O content of the melt based on the EMPA total before the normalization to dry, including a correction for 0.6 wt % Na_2O loss
[8]Theoretical H_2O content of the melt, calculated from the total H_2O of the charge and the volume percent crystals
[9]Assuming the same discrepancy between 'H_2O by difference' and 'H_2O by FTIR' as in Anhy-5
amph, amphibole; anhy, anhydrite; mgt, magnetite; n.a., not analyzed; N/A, not applicable

into hydrous minerals, but these factors are unlikely to affect the result by more than 20%. Therefore, as pointed out by Zajacz & Tsay (2019), any oxidized arc basaltic liquid should theoretically reach anhydrite saturation during its fractionation to high-silica andesitic composition. The fact that our two most hydrous experiments returned considerably higher anhydrite solubilities than what is predicted by the model of Zajacz & Tsay (2019) does not alter this conclusion. The mere presence of anhydrite in a natural arc magma is thus probably not unusual, and we expect that many more occurrences of magmatic anhydrite will be found worldwide if more specifically searched for. However, sulfur contents greater than ~0.3 wt % S in (trachy-)andesitic to (trachy-)dacitic magmas may be indeed uncommon and reflect magma fractionation at high pressure, which factor has been identified to be critical in the formation of porphyry Cu deposits (Loucks, 2021). Common anhydrite saturation in arc magmas has also important implications for the 'excess sulfur' phenomenon during volcanic eruptions, as excess sulfur can be contributed via breakdown of anhydrite.

CONCLUSIONS

The following conclusions can be drawn from this study:

(1) The former presence of anhydrite phenocrysts in porphyritic magmas can be recognized through cavities that show a strong spatial association with apatite phenocrysts. These cavities can be either empty or they can be filled with low-T secondary minerals such as carbonates, zeolites or microcrystalline SiO_2.
(2) Direct evidence for magmatic anhydrite saturation is provided by anhydrite inclusions preserved within other phenocrysts. Apatite is a particularly common host of anhydrite inclusions.
(3) The common coexistence of the anhydrite with MSS suggests magma oxygen fugacities 2.0 ± 0.5 log units above the FMQ buffer.
(4) In samples with particularly well-recognizable former anhydrite phenocrysts, their modal abundance can be quantified based on high-resolution scans of polished hand specimens.

The results obtained from three of our samples suggest minimum magma sulfur contents of 0.20 to 0.56 wt % S.

(5) The highest sulfur content is difficult to reconcile with existing anhydrite solubility models, but it could be reproduced in an experiment performed at 950°C and 1.15 GPa on a natural latitic melt with 13 wt % H_2O.

(6) The above results suggest that the natural latitic magma with 0.56 wt % S must have been extremely hydrous and thus have formed via magma fractionation at high pressure (probably ≥1.0 GPa).

(7) Whereas arc magmas are expected to commonly reach anhydrite saturation at >60 wt % SiO_2 in the silicate melt, sulfur contents greater than ∼0.3 wt % S can probably be reached only in magmas that fractionate at pressures greater than ∼0.5 GPa. In this respect, the occurrence of magmas with up to 0.56 wt % S in the Central Mining District fits with the strong association of porphyry-Cu deposits with high-Sr/Y magmas, which geochemical signature is indicative of magma fractionation at high pressure.

SUPPLEMENTARY DATA

Supplementary data are available at *Journal of Petrology* online.

Acknowledgements

We like to thank Mac Canby, Angela Roach, Garret Brinkerhoff and Hunter England from Freeport-McMoRan for access and guiding in the Santa Rita pit, Detlef Krauße for help with the electron microprobe analyses, Hans Keppler for help with the FTIR analyses, and Raphael Njul for help with the sample preparation. Sincere thanks also to Zoltan Zajacz, Matteo Masotta, Celestine Mercer (USGS), Katrina Sauer (USGS) and an anonymous reviewer for their very helpful comments, and to Associate Editor Christina Wang for handling the manuscript. Any use of trade, firm, or product names is for descriptive purposes only and does not imply endorsement by the U.S. Government.

Data Availability

The whole-rock data were deposited in the EarthChem Library (DOI: 10.60520/IEDA/113392; https://ecl.earthchem.org/view.php?id=3392; Supplementary Table S1).

REFERENCES

Arculus, R. J., Johnson, R. W., Chappell, B. W., McKee, C. O. & Sakai, H. (1983). Ophiolite-contaminated andesites, trachybasalts, and cognate inclusions of mount lamington, Papua New Guinea: anhydrite-amphibole-bearing lavas and the 1951 cumulodome. *Journal of Volcanology and Geothermal Research* **18**, 215–247. https://doi.org/10.1016/0377-0273(83)90010-0.

Audétat, A. & Bali, E. (2010). A new technique to seal volatile-rich samples into platinum capsules. *European Journal of Mineralogy* **22**, 23–27. https://doi.org/10.1127/0935-1221/2010/0022-1982.

Audétat, A. & Pettke, T. (2006). Evolution of a porphyry-Cu mineralized magma system at Santa Rita, New Mexico (U.S.A.). *Journal of Petrology* **47**, 2021–2046. https://doi.org/10.1093/petrology/egl035.

Audétat, A. & Simon, A. C. (2012) Magmatic controls on porphyry Cu genesis. In: Hedenquist J. W., Harris M. & Camus F. (eds) *Geology and genesis of major copper deposits and districts of the world: a tribute to Richard Sillitoe*, Vol. **16**. Littleton, CO: Society of Economic Geologists, Special Publication, pp.553–572.

Audétat, A., Pettke, T. & Dolejs, D. (2004). Magmatic anhydrite and calcite in the ore-forming quartz-monzodiorite magma at Santa Rita, New Mexico (USA): genetic constraints on porphyry-Cu mineralization. *Lithos* **72**, 147–161. https://doi.org/10.1016/j.lithos.2003.10.003.

Bacon, C. R. & Hirschmann, M. M. (1988). Mg/Mn partitioning test for equilibrium between coexisting Fe–Ti oxides. *American Mineralogist* **73**, 57–61.

Barber, N. D., Edmonds, M., Jenner, F., Audétat, A. & Williams, H. (2021). Amphibole control on copper systematics in arcs: insights from the analysis of global datasets. *Geochimica et Cosmochimica Acta* **307**, 192–211. https://doi.org/10.1016/j.gca.2021.05.034.

Barth, A. P. & Dorais, M. J. (2000). Magmatic anhydrite in granitic rocks: first occurrence and petrological consequences. *American Mineralogist* **85**, 430–435. https://doi.org/10.2138/am-2000-0404.

Beccaluva, L., Gabbianelli, G., Lucchini, F., Rossi, P. L. & Savelli, C. (1985). Petrology and K/Ar ages of volcanics dredged from the Eolian seamounts: implications for geodynamic evolution of the southern Tyrrhenian basin. *Earth and Planetary Science Letters* **74**, 187–208. https://doi.org/10.1016/0012-821X(85)90021-4.

Behrens, H., Tamic, N. & Holtz, F. (2004). Determination of the molar absorption coefficient for the infrared absorption band of CO_2 in rhyolitic glasses. *American Mineralogist* **89**, 301–306. https://doi.org/10.2138/am-2004-2-307.

Bénard, A., Klimm, K., Woodland, A. B., Arculus, R. J., Wilke, M., Botcharnikov, R. E., Shimizu, N., Nebel, O., Rivard, C. & Ionov, D. A. (2018). Oxidising agents in sub-arc mantle melts link slab devolatilisation and arc magmas. *Nature Communications* **9**, 3500. https://doi.org/10.1038/s41467-018-05804-2.

Bernard, A., Demaiffe, D., Mattielli, N. & Punongbayan, R. S. (1991). Anhydrite-bearing pumice from Mount Pinatubo: further evidence for the existence of sulphur-rich silicic magmas. *Nature* **354**, 139–140. https://doi.org/10.1038/354139a0.

Botcharnikov, R. E., Linnen, R. L., Wilke, M., Holtz, F., Jugo, P. J. & Berndt, J. (2011). High gold concentrations in sulphide-bearing magma under oxidizing conditions. *Nature Geoscience* **4**, 112–115. https://doi.org/10.1038/ngeo1042.

Brandl, P. A., Portnyagin, M., Zeppenfeld, H., Tepley, F. J., III, de Ronde, C. E. J., Timm, C., Hauff, F., Garbe-Schönberg, D. & Bousquet, R. (2023). The origin of magmas and metals at the submarine Brothers Volcano, Kermadec Arc, New Zealand. *Economic Geology* **118**, 1577–1604. https://doi.org/10.5382/econgeo.4973.

Calvo, L. M. (2022) *Volatile and trace element partitioning during arc magma fractionation in the lower crust*. Unpublished M.Sc. thesis. Bayreuth: University of Bayreuth, p.73.

Cao, M., Hollings, P., Cooke, D. R., Evans, N. J., McInnes, B. I. A., Qin, K., Li, G., Sweet, G. & Baker, M. (2018). Physicochemical processes in the magma chamber under the Black Mountain porphyry Cu–Au deposit, Philippines: insights from mineral chemistry and implications for mineralization. *Economic Geology* **113**, 63–82. https://doi.org/10.5382/econgeo.2018.4544.

Cernuschi, F., Dilles, J. H., Osorio, J., Proffett, J. M. & Kouzmanov, K. (2023). A reevaluation of the timing and temperature of copper and molybdenum precipitation in porphyry deposits. *Economic Geology* **118**, 931–902. https://doi.org/10.5382/econgeo.5032.

Chambefort, I., Dilles, J. H. & Kent, A. J. R. (2008). Anhydrite-bearing andesite and dacite as a source for sulfur in magmatic-hydrothermal mineral deposits. *Geology* **36**, 719–722. https://doi.org/10.1130/G24920A.1.

Chang, J. & Audétat, A. (2018). Petrogenesis and metal content of hornblende-rich xenoliths from two Laramide-age magma

systems in southwestern USA: insights into the metal budget of arc magmas. *Journal of Petrology* **59**, 1869–1898. https://doi.org/10.1093/petrology/egy083.

Chang, J., Li, J. W. & Audétat, A. (2018). Formation and evolution of multistage magmatic-hydrothermal fluids at the Yulong porphyry Cu–Mo deposit, eastern Tibet: insights from LA-ICP-MS analysis of fluid inclusions. *Geochimica et Cosmochimica Acta* **232**, 181–205. https://doi.org/10.1016/j.gca.2018.04.009.

Chiaradia, M. (2014). Copper enrichment in arc magmas controlled by overriding plate thickness. *Nature Geoscience* **7**, 43–46. https://doi.org/10.1038/ngeo2028.

Chiaradia, M. & Caricchi, L. (2017). Stochastic modelling of deep magmatic controls on porphyry copper deposit endowment. *Scientific Reports* **7**, 44523. https://doi.org/10.1038/srep44523.

Core, D., Kesler, S. & Essene, E. (2001) Magmatic anhydrite in the Hanover-Fierro stock and its implications for fS_2-fO_2 of intrusions associated with porphyry copper deposits. In: *Geological Society of America, 2001 annual meeting, Abstracts with programs*, Vol. **33**. Boulder: Geological Society of America, pp.357–358.

Creaser, E. C., Steele-MacInnis, M. & Tutolo, B. M. (2022). A model for the solubility of anhydrite in H_2O-NaCl fluids from 25 to 800 °C, 0.1 to 1400 MPa, and 0 to 60 wt% NaCl: applications to hydrothermal ore-forming systems. *Chemical Geology* **587**, 120609. https://doi.org/10.1016/j.chemgeo.2021.120609.

Dilles, J. H., Kent, A. J. R., Wooden, J. L., Tosdal, R. M., Koleszar, A., Lee, R. G. & Farmer, L. (2015). Zircon compositional evidence for sulfur-degassing from ore-forming arc magmas. *Economic Geology* **110**, 241–251. https://doi.org/10.2113/econgeo.110.1.241.

Dirksen, O., Humphreys, M. C. S., Pletchov, P., Melnik, O., Demyanchuk, Y., Sparks, R. S. J. & Mahony, S. (2006). The 2001–2004 dome-forming eruption of Shiveluch volcano, Kamchatka: observation, petrological investigation and numerical modelling. *Journal of Volcanology and Geothermal Research* **155**, 201–226. https://doi.org/10.1016/j.jvolgeores.2006.03.029.

Drexler, J. W. & Munoz, J. L. (1985) Highly oxidized, pyrrhotite-anhydrite-bearing silicic magmas from the Julcani Ag–Cu–Bi–Pb–Au–W district, Peru: physicochemical conditions of a productive magma. In: Taylor, R. P. & Strong, D. F. (eds) *Canadian Institute of Mining conference on granite-related mineral deposits, Halifax September 15–17, 1985, Extended Abstracts*. Canadian Institute of Mining and Metallurgy, pp.87–100.

Einaudi, M. T. (1982) Description of skarns associated with porphyry copper plutons, Southwestern North America. In: Titley S. R. (ed) *Advances in the geology of the porphyry copper deposits, Southwestern North America*. Tucson: University of Arizona Press, pp.239–284.

Evans, H. T. (1979). The thermal expansion of anhydrite to 1000°C. *Physics and Chemistry of Minerals* **4**, 77–82. https://doi.org/10.1007/BF00308361.

Evans, K. A., Elburg, M. A. & Kamenetsky, V. S. (2012). Oxidation state of subarc mantle. *Geology* **40**, 783–786. https://doi.org/10.1130/G33037.1.

Fournelle, J., Carmody, R. & Daag, A. S. (1996) Anhydrite-bearing pumices from the June 15, 1991, eruption of Mt. Pinatubo: geochemistry, mineralogy, and petrology. In: Newhall C. G. & Punongbayan R. S. (eds) *Fire and mud: eruptions and lahars of Mount Pinatubo, Philippines*. Seattle: University of Washington Press, pp.845–862.

Freise, M., Holtz, F., Nowak, M., Scoates, J. S. & Strauss, H. (2009). Differentiation and crystallization conditions of basalts from the Kerguelen large igneous province: an experimental study. *Contributions to Mineralogy and Petrology* **158**, 505–527. https://doi.org/10.1007/s00410-009-0394-5.

Ghiorso, M. S. & Evans, B. W. (2008). Thermodynamics of rhombohedral oxide solid solutions and a revision of the Fe–Ti two-oxide geothermometer and oxygen-barometer. *American Journal of Science* **308**, 957–1039. https://doi.org/10.2475/09.2008.01.

Grondahl, C. & Zajacz, Z. (2017). Magmatic controls on the genesis of porphyry Cu–Mo–Au deposits: the Bingham Canyon example. *Earth and Planetary Science Letters* **480**, 53–65. https://doi.org/10.1016/j.epsl.2017.09.036.

Gurenko, A. (2021). Origin of sulphur in relation to silicate-sulphide immiscibility in Tolbachik primitive arc magma (Kamchatka, Russia): insights from sulphur and boron isotopes. *Chemical Geology* **576**, 120244. https://doi.org/10.1016/j.chemgeo.2021.120244.

Gustafson, L. B. & Hunt, J. P. (1975). The porphyry copper deposit at El Salvador, Chile. *Economic Geology* **70**, 857–912. https://doi.org/10.2113/gsecongeo.70.5.857.

Hacker, B. R. & Abers, G. A. (2004). Subduction factory 3: an excel worksheet and macro for calculating the densities, seismic wave speeds, and H_2O contents of minerals and rocks at pressure and temperature. *Geochemistry, Geophysics, Geosystems* **5**. https://doi.org/10.1029/2003GC000614.

Hannink, R. L. (2010) *Mineralization and timing of the Lover's Lane breccia, Santa Rita porphyry Cu–Mo Deposit, Grant County, New Mexico*. Published M.Sc. thesis,. Reno: University of Nevada, p.155.

Harrison, T. M. & Watson, E. B. (1984). The behavior of apatite during crustal anatexis: equilibrium and kinetic considerations. *Geochimica et Cosmochimica Acta* **48**, 1467–1477. https://doi.org/10.1016/0016-7037(84)90403-4.

Hernon, R. M. & Jones, W. R. (1986) Ore deposits of the Central Mining District, Grant County, New Mexico. In: Ridge J. (ed) *Ore deposits of the United States, 1933–1976*. New York: The American Institute of Mining, Metallurgical, and Petroleum Engineers Inc., pp.1211–1238.

Hernon, R. M., Jones, W. R. & Moore, S. L. (1964) *Geology of the Santa Rita Quadrangle, New Mexico. 1:24.000*. Washington: U. S. Geological Survey.

Hillesland, L. L., Hawkins, R. B. & Worthington, W. T. (1995) The geology and mineralization of the Continental mine area, Grant County, New Mexico. In: Pierce F. W. & Bolm J. G. (eds) *Porphyry copper deposits of the American Cordillera*, Vol. **20**. Tucson: Arizona Geological Society Digest, pp.473–483.

Huber, C., Townsend, M., Degruyter, W. & Bachmann, O. (2019). Optimal depth of subvolcanic magma chamber growth controlled by volatiles and crust rheology. *Nature Geoscience* **12**, 762–768. https://doi.org/10.1038/s41561-019-0415-6.

Hunt, J. P. (1991). Porphyry copper deposits. *Economic Geology Monograph* **8**, 192–206. https://doi.org/10.5382/Mono.08.09.

Hutchinson, M. C. & Dilles, J. H. (2019). Evidence for magmatic anhydrite in porphyry copper intrusions. *Economic Geology* **114**, 143–152. https://doi.org/10.5382/econgeo.2019.4624.

Iacovino, K. & Till, C. B. (2019). DensityX: a program for calculating the densities of magmatic liquids up to 1,627 °C and 30 kbar. *Volcanica* **2**, 1–10. https://doi.org/10.30909/vol.02.01.0110.

Imai, A., Listanco, E. L. & Fujii, T. (1993). Petrologic and sulfur isotopic significance of highly oxidized and sulfur-rich magma of Mt. Pinatubo, Philippines. *Geology* **21**, 699–702. https://doi.org/10.1130/0091-7613(1993)021<0699:PASISO>2.3.CO;2.

Jenner, F. E. (2017). Cumulate causes for the low contents of sulfide-loving elements in the continental crust. *Nature Geoscience* **10**, 524–529. https://doi.org/10.1038/ngeo2965.

Jenner, F. E., O'Neill, H. C., Arculus, R. J. & Mavrogenes, J. A. (2010). The magnetite crisis in the evolution of arc-related magmas and the initial concentrations of Au, Ag and Cu. *Journal of Petrology* **51**, 2445–2464. https://doi.org/10.1093/petrology/egq063.

Jenner, F. E., Hauri, E. H., Bullock, E. S., König, S., Arculus, R. J., Mavrogenes, J. A., Mikkelson, N. & Goddard, C. (2015). The competing effects of sulfide saturation versus degassing on the behavior of the chalcophile elements during the differentiation of hydrous melts. *Geochemistry Geophysics Geosystems* **16**, 1490–1507. https://doi.org/10.1002/2014GC005670.

Jones, W. R., Hernon, R. M. & Moore, S. L. (1967) *General geology of the Santa Rita quadrangle, Grant country, New Mexico*, Vol. **555**. Washington: U. S. Geological Survey. Professional Paper, p.144.

Jugo, P. J., Wilke, M. & Botcharnikov, R. E. (2010). Sulfur K-edge XANES analysis of natural and synthetic basaltic glasses: implications for S speciation and S content as function of oxygen fugacity. *Geochimica et Cosmochimica Acta* **74**, 5926–5938. https://doi.org/10.1016/j.gca.2010.07.022.

Keith, M., Haase, K. M., Klemd, R., Smith, D. J., Schwarz-Schampera, U. & Bach, W. (2018). Constraints on the source of Cu in a submarine magmatic-hydrothermal system, Brothers volcano, Kermadec island arc. *Contributions to Mineralogy and Petrology* **173**, 40. https://doi.org/10.1007/s00410-018-1470-5.

Kleinsasser, J. M., Simon, A. C., Konecke, B. A., Kleinsasser, M. J., Beckmann, P. & Holtz, F. (2022). Sulfide and sulfate saturation of dacitic melts as a function of oxygen fugacity. *Geochimica et Cosmochimica Acta* **326**, 1–16. https://doi.org/10.1016/j.gca.2022.03.032.

Klimm, K., Kohn, S. C. & Botcharnikov, R. E. (2012). The dissolution mechanism of sulphur in hydrous silicate melts. II: solubility and speciation of sulphur in hydrous silicate melts as a function of fO_2. *Chemical Geology* **322-323**, 250–267. https://doi.org/10.1016/j.chemgeo.2012.04.028.

Le Bas, M. J., Le Maitre, R. W., Streckeisen, A. & Zanettin, B. (1986). A chemical classification of volcanic rocks based on the total alkali-silica diagram. *Journal of Petrology* **27**, 745–750. https://doi.org/10.1093/petrology/27.3.745.

Lee, C.-T. A. & Tang, M. (2020). How to make porphyry copper deposits. *Earth and Planetary Science Letters* **529**, 115868. doi.org/10.1016/j.epsl.2019.115868.

Lee, C.-T. A., Luffi, P., Chin, E. J., Bouchet, R., Dasgupta, R., Morton, D. M., Le Roux, V., Xin, Q.-Z. & Jin, D. (2012). Copper systematics in arc magmas and implications for crust-mantle differentiation. *Science* **336**, 64–68. https://doi.org/10.1126/science.1217313.

Li, Y. & Audétat, A. (2015). Effects of temperature, silicate melt composition, and oxygen fugacity on the partitioning of V, Mn, Co, Ni, Cu, Zn, As, Mo, Ag, Sn, Sb, W, Au, Pb, and Bi between sulfide phases and silicate melt. *Geochimica et Cosmochimica Acta* **162**, 25–45. https://doi.org/10.1016/j.gca.2015.04.036.

Li, Y., Feng, L., Kiseeva, E. S., Gao, Z., Guo, H., Du, Z., Wang, F. & Shi, L. (2019). An essential role for sulfur in sulfide-silicate melt partitioning of gold and magmatic gold transport at subduction settings. *Earth and Planetary Science Letters* **528**, 115850. https://doi.org/10.1016/j.epsl.2019.115850.

Li, J., Li, G., Evans, N. J., Zhao, J., Qin, K. & Xie, J. (2021). Primary fluid exsolution in porphyry copper systems: evidence from magmatic apatite and anhydrite inclusions in zircon. *Mineralium Deposita* **56**, 407–415. https://doi.org/10.1007/s00126-020-01013-4.

Lickfold, V., Cooke, D. R., Smith, S. G. & Ullrich, T. D. (2003). Endeavour copper-gold porphyry deposits, Northparkes, New South Wales: intrusive history and fluid evolution. *Economic Geology* **98**, 1607–1636. https://doi.org/10.2113/gsecongeo.98.8.1607.

Liu, K., Zhang, L. & Ni, H. (2023). Anhydrite solubility enhanced by CaO in silicate melts: implications for sulfur cycling in subduction zones. *Geochimica et Cosmochimica Acta* **349**, 135–145. https://doi.org/10.1016/j.gca.2023.04.007.

Loucks, R. R. (2014). Distinctive composition of copper-ore-forming arc magmas. *Australian Journal of Earth Sciences* **61**, 5–16. https://doi.org/10.1080/08120099.2013.865676.

Loucks, R. L. (2021). Deep entrapment of buoyant magmas by orogenic tectonic stress: its role in producing continental crust, adakites, and porphyry copper deposits. *Earth Science Reviews* **220**, 103744. https://doi.org/10.1016/j.earscirev.2021.103744.

Loucks, R. L. & Fiorentini, M. L. (2023). Early zircon saturation in adakitic magmatic differentiation series and low Zr content of porphyry copper magmas. *Mineralium Deposita* **58**, 1381–1393. https://doi.org/10.1007/s00126-023-01208-5.

Lu, Y.-J., Loucks, R. L., Fiorentini, M. L., Yang, Z.-M. & Hou, Z.-Q. (2015). Fluid flux melting generated postcollisional high Sr/Y copper ore-forming water-rich magmas in Tibet. *Geology* **43**, 583–586. https://doi.org/10.1130/G36734.1.

Luhr, J. F. (1990). Experimental phase relations of water- and sulfur-saturated arc magmas and the 1982 eruptions of El Chichón volcano. *Journal of Petrology* **31**, 1071–1114. https://doi.org/10.1093/petrology/31.5.1071.

Luhr, J. F. (2008). Primary igneous anhydrite: progress since its recognition in the 1982 El Chichón trachyandesite. *Journal of Volcanological and Geothermal Research* **175**, 394–407. https://doi.org/10.1016/j.jvolgeores.2008.02.016.

Luhr, J. F. & Melson, W. G. (1996) Mineral and glass compositions in June 15, 1991, pumices: evidence for dynamic disequilibrium in the dacite of Mount Pinatubo. In: Newhall C. G. & Punongbayan R. S. (eds) *Fire and mud: eruptions and lahars of the Mount Pinatubo, Philippines*. Seattle: Univ. Washington Press, pp.733–750.

Luhr, J. F., Carmichael, I. S. E. & Varekamp, J. C. (1984). The 1982 eruptions of El Chichón Volcano, Chiapas, Mexico: mineralogy and petrology of the anhydrite-bearing pumices. *Journal of Volcanological and Geothermal Research* **23**, 69–108. https://doi.org/10.1016/0377-0273(84)90057-X.

Matjuschkin, V., Blundy, J. D. & Brooker, R. A. (2016). The effect of pressure on sulphur speciation in mid- to deep-crustal arc magmas and implications for the formation of porphyry copper deposits. *Contributions to Mineralogy and Petrology* **171**, 66. https://doi.org/10.1007/s00410-016-1274-4.

Matthews, S. J., Jones, A. P. & Gardeweg, M. C. (1994). Lascar Volcano, Northern Chile: evidence for steady-state disequilibrium. *Journal of Petrology* **35**, 401–432. https://doi.org/10.1093/petrology/35.2.401.

Matthews, S. J., Gardeweg, M. C. & Sparks, R. S. J. (1997). The 1984 to 1996 cyclic activity of Lascar Volcano, northern Chile: cycles of dome growth, dome subsidence, degassing and explosive eruptions. *Bulletin of Volcanology* **59**, 72–82. https://doi.org/10.1007/s004450050176.

McDonald, G. A. & Katsura, T. (1964). Chemical composition of Hawaiian lavas. *Journal of Petrology* **5**, 82–133. https://doi.org/10.1093/petrology/5.1.82.

McDowell, F. W. (1971). K-Ar ages of igneous rocks from the western United States. *Isochron/West* **2**, 1–16.

Melson, W. G., Allan, J. F., Reid Jerez, D., Nelen, J., Clavache, M. L., Williams, S. N., Fournelle, J. & Perfit, M. (1990). Water contents, temperature and diversity of the magmas of the catastrophic eruption of Nevado del Ruiz, Colombia, November 13, 1985. *Journal of Volcanology and Geothermal Research* **41**, 97–126. https://doi.org/10.1016/0377-0273(90)90085-T.

Métrich, N. & Wallace, P. J. (2008) Volatile abundances in basaltic magmas and their degassing paths tracked by melt inclusions. In: Putirka K. D. & Tepley F. J. I. (eds) *Minerals, inclusions and volcanic processes*. Chantilly: Mineralogical Society of America, pp.363–402. https://doi.org/10.1515/9781501508486-011.

Mizer, J. D., Barton, M. D. & Stegen, R. J. (2015) U-Pb Geochronology of Laramide magmatism related to Cu-, Zn-, and Fe-mineralized systems, Central Mining District, New Mexico. In: Pennell W. M. & Garside L. J. (eds) *New concepts and discoveries, Geological Society of Nevada Symposium May 14–23 Reno Conference Proceedings*, Vol. **2**. Lancaster, USA: DEStech Publications, Inc., pp.1109–1129.

Morizet, Y., Brooker, R. A. & Kohn, S. C. (2002). CO_2 in haplo-phonolite melt: solubility, speciation and carbonate complexation. *Geochimica et Cosmochimica Acta* **66**, 1809–1820. https://doi.org/10.1016/S0016-7037(01)00893-6.

Moss, R., Scott, S. D. & Binns, R. A. (2001). Gold content of Eastern Manus Basin volcanic rocks: implications for enrichment in associated hydrothermal precipitates. *Economic Geology* **96**, 91–107. https://doi.org/10.2113/96.1.91.

Mutschler, F. E., Ludington, S. & Bookstrom, A. A. (1999). Giant porphyry-related metal camps of the world - a database. In: *U.S. Geological Survey Open-File Report* **99–556**, *Online Version* 1.0. Available at: http://geopubs.wr.usgs.gov/open-file/of99-556/ {Accessed January 2006}.

Nandedkar, R. H., Ulmer, P. & Müntener, O. (2014). Fractional crystallization of primitive, hydrous arc magmas: an experimental study at 0.7 GPa. *Contributions to Mineralogy and Petrology* **167**, 1015. https://doi.org/10.1007/s00410-014-1015-5.

Nathwani, C., Blundy, J., Large, S. J. E., Wilkinson, J. J., Buret, Y., Loader, M. A., Tavazzani, L. & Chelle-Michou, C. (2024). A zircon case for super-wet arc magmas. *Nature Communications* **15**, 8982. https://doi.org/10.1038/s41467-024-52786-5.

Nowak, M., Porbatzki, D., Spickenbom, K. & Diedrich, O. (2003). Carbon dioxide speciation in silicate melts: a restart. *Earth and Planetary Science Letters* **207**, 131–139. https://doi.org/10.1016/S0012-821X(02)01145-7.

Ohlhorst, S., Behrens, H. & Holtz, F. (2001). Compositional dependence of molar absorptivities of near-infrared OH- and H_2O bands in rhyolitic to basaltic glasses. *Chemical Geology* **174**, 5–20. https://doi.org/10.1016/S0009-2541(00)00303-X.

Pallister, J. S., Hoblitt, R. P., Meeker, G. P., Knight, R. J. & Siems, D. F. (1996) Magma mixing at Mount Pinatubo: petrographic and chemical evidence from the 1991 deposits. In: Newhall C. G. & Punongbayan R. S. (eds) *Fire and mud: eruptions and lahars of Mount Pinatubo, Philippines*. Seattle: University of Washington Press, pp.687–731.

Parat, F., Dungan, M. & Streck, M. J. (2002). Anhydrite, pyrrhotite and sulfur-rich apatite: tracing the sulfur evolution of an Oligocene andesite (Eagle Mountain, CO, USA). *Lithos* **64**, 63–75. https://doi.org/10.1016/S0024-4937(02)00155-X.

Parat, F., Dungan, M. A. & Lipman, P. W. (2005). Contemporaneous trachyandesitic and calc-alkaline volcanism of the Huerto Andesite, San Juan Volcanic Field, Colorado, USA. *Journal of Petrology* **46**, 859–891. https://doi.org/10.1093/petrology/egi003.

Parat, F., Holtz, F. & Feig, S. (2008). Pre-eruptive conditions of the Huerto Andesite (Fish Canyon System, San Juan Volcanic Field, Colorado): influence of volatiles (C–O–H–S) on phase equilibria and mineral composition. *Journal of Petrology* **49**, 911–935. https://doi.org/10.1093/petrology/egn011.

Parat, F., Holtz, F. & Streck, M. J. (2011). Sulfur-bearing magmatic accessory minerals. *Reviews in Mineralogy and Geochemistry* **73**, 285–314. https://doi.org/10.2138/rmg.2011.73.10.

Park, J.-W., Campbell, I. H., Kim, J. & Moon, J.-W. (2015). The role of late sulfide saturation in the formation of a Cu- and Au-rich magma: insights from the platinum-group geochemistry of Niuatahi-Motutahi lavas, Tonga rear arc. *Journal of Petrology* **56**, 59–81. https://doi.org/10.1093/petrology/egu071.

Plank, T., Kelley, K. A., Zimmer, M. M., Hauri, E. H. & Wallace, P. J. (2013). Why do mafic arc magmas contain ~4 wt% water on average? *Earth and Planetary Science Letters* **364**, 168–179. https://doi.org/10.1016/j.epsl.2012.11.044.

Pribavkin, S. V., Avdonina, I. S. & Zamyatin, D. A. (2013). Mineralogy, conditions of crystallization and melt generation of epidote-bearing porphyries from the Middle Urals, Russian Federation. *Mineralogy and Petrology* **107**, 125–147. https://doi.org/10.1007/s00710-012-0226-6.

Rasmussen, D. J., Plank, T. A., Roman, D. C. & Zimmer, M. M. (2022). Magmatic water content controls the pre-eruptive depth of arc magmas. *Science* **375**, 1169–1172. https://doi.org/10.1126/science.abm5174.

Rose, W. I., Bornhorst, T. J., Halsor, S. P., Capaul, W. A., Plumley, P. S., Servando de la Cruz-Reyna, M. M. & Mota, R. (1984). Volcán El Chichón, Mexico: pre-1982 S-rich eruptive activity. *Journal of Volcanology and Geothermal Research* **23**, 147–167. https://doi.org/10.1016/0377-0273(84)90060-X.

Rottier, B., Kouzmanov, K., Ovtcharova, M., Ulianov, A., Wälle, M., Selby, D. & Fontboté, L. (2020). Multiple rejuvenation episodes of a silicic magma reservoir at the origin of the large diatreme-dome complex and porphyry-type mineralization events at Cerro de Pasco (Peru). *Lithos* **376-377**, 105766. https://doi.org/10.1016/j.lithos.2020.105766.

Sadofsky, S. J., Portnyagin, M., Hoernle, K. & Van den Bogaard, P. (2008). Subduction cycling of volatiles and trace elements through the Central American volcanic arc: evidence from melt inclusions. *Contributions to Mineralogy and Petrology* **155**, 433–456. https://doi.org/10.1007/s00410-007-0251-3.

Schmidt, M. W. & Jagoutz, O. (2017). The global systematics of primitive arc melts. *Geochemistry Geophysics Geosystems* **18**, 2817–2854. https://doi.org/10.1002/2016GC006699.

Shinohara, H. (2013). Volatile flux from subduction zone volcanoes: insights from a detailed evaluation of the fluxes from volcanoes in Japan. *Journal of Volcanological and Geothermal Research* **268**, 46–63. https://doi.org/10.1016/j.jvolgeores.2013.10.007.

Sillitoe, R. H. (2010). Porphyry copper systems. *Economic Geology* **105**, 3–41. https://doi.org/10.2113/gsecongeo.105.1.3.

Singer, D. A., Berger, V. I. & Moring, B. C. (2008) Porphyry copper deposits of the world: database and grade and tonnage models, 2008. In: *U.S. Geological Survey Open-File Report 2008–11155*, 45 pp.

Stern, C. R., Funk, J. A., Skewes, M. A. & Arévalo, A. (2007). Magmatic anhydrite in plutonic rocks at the El Teniente Cu–Mo deposit, Chile, and the role of sulfur- and copper-rich magmas in its formation. *Economic Geology* **102**, 1335–1344. https://doi.org/10.2113/gsecongeo.102.7.1335.

Sulaksono, A., Watanabe, Y., Arribas, A., Echigo, T., Al Furqan, R. & Leys, C. A. (2021). Reduction of oxidized sulfur in the formation of the Grasberg porphyry copper-gold deposit, Papua, Indonesia. *Mineralium Deposita* **56**, 1027–1042. https://doi.org/10.1007/s00126-021-01040-9.

Swanson, S. E. & Kearney, C. S. (2008). Anhydrite in the 1989-1990 lavas and xenoliths from Redoubt volcano, Alaska. *Journal of Volcanology and Geothermal Research* **175**, 509–516. https://doi.org/10.1016/j.jvolgeores.2008.02.027.

Thoman, M. W., North, R. M. & Worthington, W. T. (2006). *Santa Rita porphyry copper deposit, Grant County, New Mexico*. In: *Guidebook for the Arizona Geological Society fall field trip, November 4–5, 2006*. Arizona Geological Society, p.55.

Ulmer, P., Kaegi, R. & Müntener, O. (2018). Experimentally derived intermediate to silica-rich arc magmas by fractional and equilibrium crystallization at 1.0 GPa: an evaluation of phase

relationships, compositions, liquid lines of descent and oxygen fugacity. *Journal of Petrology* **59**, 11–58. https://doi.org/10.1093/petrology/egy017.

Wallace, P. J. (2005). Volatiles in subduction zone magmas: concentrations and fluxes based on melt inclusion and volcanic gas data. *Journal of Volcanological and Geothermal Research* **140**, 217–240. https://doi.org/10.1016/j.jvolgeores.2004.07.023.

Wallace, P. J. & Edmonds, M. (2011). The sulfur budget in magmas: evidence from melt inclusions, submarine glasses, and volcanic gas emissions. *Reviews in Mineralogy and Geochemistry* **73**, 215–246. https://doi.org/10.2138/rmg.2011.73.8.

Xiao, B., Qin, K., Li, G., Li, J., Xia, D., Chen, L. & Zhao, J. (2012). Highly oxidized magma and fluid evolution of Miocene Qulong giant porphyry Cu–Mo deposit, southern Tibet, China. *Resource Geology* **62**, 4–18. https://doi.org/10.1111/j.1751-3928.2011.00177.x.

Xu, Z. & Li, Y. (2021). The sulfur concentration at anhydrite saturation in silicate melts: implications for sulfur cycle and oxidation state in subduction zones. *Geochimica et Cosmochimica Acta* **306**, 98–123. https://doi.org/10.1016/j.gca.2021.05.027.

Xu, T., Liu, X., Xiong, X. & Wang, J. (2022). Sulfur dissolution capacity of highly hydrated and fluid-saturated dacitic magmas at the lower crust and implications for porphyry deposit formation. *Geochimica et Cosmochimica Acta* **333**, 107–123. https://doi.org/10.1016/j.gca.2022.07.004.

Zajacz, Z. & Tsay, A. (2019). An accurate model to predict sulfur concentration at anhydrite saturation in silicate melts. *Geochimica et Cosmochimica Acta* **261**, 288–304. https://doi.org/10.1016/j.gca.2019.07.007.

Zhang, D. & Audétat, A. (2017). What caused the formation of the giant Bingham canyon porphyry Cu–Mo–Au deposit? Insights from melt inclusions and magmatic sulfides. *Economic Geology* **112**, 221–244. https://doi.org/10.2113/econgeo.112.2.221.

Zhang, Y., Xu, Z., Zhu, M. & Wang, H. (2007). Silicate melt properties and volcanic eruptions. *Reviews in Geophysics* **45**. https://doi.org/10.1029/2006RG000216.

Journal of Petrology, 2025, **66**, egaf002
https://doi.org/10.1093/petrology/egaf002
Original Manuscript